Master's thesis

NTNU
Norwegian University of Science and Technology
Faculty of Information Technology and Electrical Engineering
Department of Electronic Systems

Gunvor Holm

Investigating domains in modified square artificial spin ice using magnetic force microscopy and simulations

Master's thesis in Nanotechnology
Supervisor: Erik Folven
Co-supervisor: Ida Breivik, Alv Johan Skarpeid
June 2023

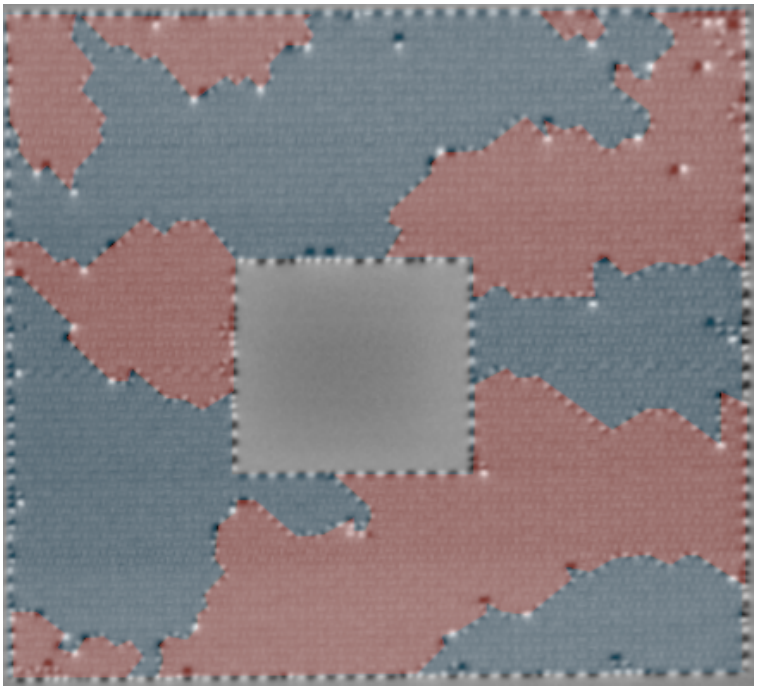

NTNU
Norwegian University of
Science and Technology

Gunvor Holm

Investigating domains in modified square artificial spin ice using magnetic force microscopy and simulations

Master's thesis in Nanotechnology
Supervisor: Erik Folven
Co-supervisor: Ida Breivik, Alv Johan Skarpeid
June 2023

Norwegian University of Science and Technology
Faculty of Information Technology and Electrical Engineering
Department of Electronic Systems

NTNU
Norwegian University of
Science and Technology

Abstract

Artificial spin ices (ASIs) are magnetic metamaterials with emergent properties that make them interesting candidates for new computing materials. Understanding more of their behavior is crucial for development of these materials for such purposes.

The goal of this thesis was to investigate properties and frustration of an annulus-shaped square ASI with a topological lattice defect enforcing the presence of a domain wall. For comparison, both structures with and without the lattice defect were studied. Investigations were performed through simulations of ASI systems using the simulator "flatspin", and through studying fabricated samples using Magnetic Force Microscopy (MFM).

All physical structures were shown to retain a number of domain walls after fabrication, which tended to form diagonally across the sample. The structures without the lattice defect always had an even number of domain walls stretching from the inner square to the outer edge, while the structures with the defect had an odd number of domain walls.

The coupling strength between the magnets in the ASI influenced how easy it was to switch the magnetization of the magnets. A weaker applied field and less applied temperature is needed to flip the magnets if their coupling strength is low. Square ASI systems with a high coupling strength showed rich domain wall dynamics in simulations.

There are still many fundamental properties of ASIs that are not yet explored. Further exploration of particularly designed ASIs and understanding such meticulously tuned structures can be useful for applications in new computational methods.

Sammendrag

Kunstige spinn-is er magnetiske metamaterialer med unike emergente egenskaper, som gjør de til gode kandidater for nye typer datamaskiner. Å forstå mer av oppførselen til disse materialene er essensielt for å utvikle de videre.

Målet med denne oppgaven var å studere en annulus-formet firkantet kunstig spinn-is med en topologisk gitterdefekt som tvinger frem en domenevegg. Både strukturer med og uten gitterdefekten ble studert for å kunne gjøre sammenligninger. Strukturene ble utforsket ved å simulere kunstige spinn-is-systemer, og gjennom å studere fysiske prøver ved hjelp av et magnetkraftmikroskop.

Alle fysiske strukturer hadde domenevegger etter fabrikasjon, som la seg diagonalt på strukturene. Strukturene uten en gitterdefekt hadde alltid et partall vegger som strakk seg fra den indre til den ytre kanten, mens strukturene med en defekt hadde et oddetall vegger.

Koblingsstyrken til magnetene i den kunstige spinn-isen påvirket hvor lett det var å bytte magnetiseringsretning i en magnet. Magneter snur magnetiseringen under lavere felt og temperatur dersom koblingsstyrken er liten. I simuleringer av firkantede kunstig spinnn-is-systemer med høy koblingsstyre var det mulig å flytte på domeneveggene.

Det er fremdeles magne fundamentale egenskaper hos kunstig spinn-is som ikke har blitt utforsket enda. Å fortsette å undersøke spesialdesignede kunstig spinn-is-strukturer kan være nyttig for bruk i nye databehandlingsmetoder.

Preface

The work presented in this 30 credits master's thesis was conducted during the spring of 2023 at the Department of Electronic Systems (IES) and concludes my five year integrated Master of Science in Nanotechnology with a specialization in Nanoelectronics. A project work doing preliminary investigations of similar structures to the ones studied in this thesis was conducted during the fall of 2022[1]. Parts of the theory and methods chapters have been reused, as they are still relevant.

Acknowledgements

I would like to thank my family, my roommates and my friends. Thank you for the support, the laughs, the hugs and all the important conversations. A special thanks to my dad for proofreading this thesis, and to Sunniva and Charlotte for the support you have given me over the past year. Thank you to my study buddy Hedda, who stuck with me across two countries. Thank you for all the more or less scientific conversations, and for showing me how to *properly* include a figure in LaTeX.

Thank you to my co-supervisors, Ida Breivik and Alv Johan Skarpeid, for your feedback, for providing help and guidance, and for being patient with me and my definition of what constitutes a "draft". Thank you to my supervisor, Erik Folven, for allowing me to work on such an interesting project, for feedback, guidance and discussions, and for being from the objectively best part of Norway.

Lastly, I want to thank Ina Fall, Cory Henry and Cory Wong, for providing motivation and mental support though their music.

Trondheim, June 8, 2023
Gunvor Holm

Contents

Chapter 1

Introduction

We are approaching a critical point when it comes to global energy consumption. Information and communication technology is one of the fastest growing energy consumers, estimated to have a yearly growth of 7%, while the worldwide energy consumption growth is expected to be 3%[2]. This trend can be opposed by creating smaller and less energy demanding transistors. However, we will soon be approaching the lower limit of transistor size.[3]. To be able to sustain our energy consumption, we are dependent on new and innovative ways to keep electrical consumption low and computing power high.

Using brains as inspiration, reservoir computing was introduced as an alternative computing method to our current binary transistor-based computers. Reservoir computing uses a non-linear reservoir layer mapping inputs to high-dimensional space to execute the computing. A readout layer transfers the resulting signals to readable output information. The reservoir layer has weighted nodes, but these weights do not need to be adjustable, in contrast to other computing models based on machine learning. Therefore, a variety of physical systems can be utilized. For hardware implementation of reservoir computing, complicated and costly methods for training are needed, whereas by using physical systems as reservoirs, real world physical phenomena can be utilized instead. Choosing the right material to use as a reservoir layer is a major challenge, as the material needs to have the ability to map to higher dimensions, have local interactions, and have global non-linear properties[4].

A promising candidate for this application is artificial spin ice (ASI)[5]. ASIs are comprised of small monodomain magnets, with emergent properties unlike those of its building blocks. Although important reservoir properties such as scalability, high number of nodes and non-linearity are satisfied in ASIs, they have not yet been realized as reservoir computers[6].

Tuning the state of an ASI is a key process for computing applications[5], and can be done through globally or locally applied magnetic fields. ASIs are highly tunable, with a large number of reachable states. However, it is difficult to retain control over the exact states of the system. One way of having more control over the magnetic states of the ASI is by tuning their geometry[7].

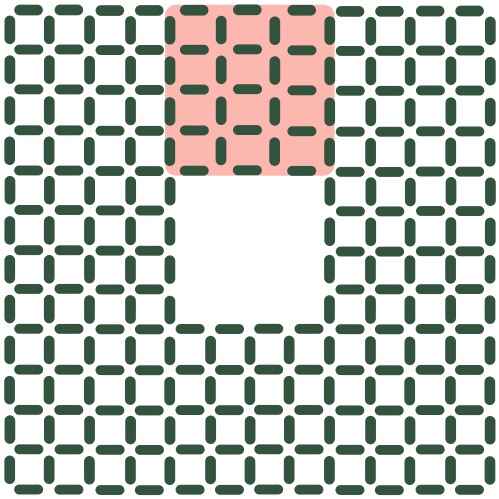

Figure 1.1: Schematic of a 12 × 12 "modified donut" square ASI with an introduced defect in the highlighted upper central part of the structure.

The goal of this thesis is to better understand the behavior of domains and domain walls in square ASI, which is a type of ASI built by combining square blocks of four magnets into a larger grid. This will be done by investigating a particular square ASI shown in figure 1.1, hereafter known as a "modified donut". By gaining more insight on domain dynamics and investigating systems with certain properties, we are getting closer to realizing artificial spin ice as a reservoir layer for reservoir computing.

1.1 Project outline

This project aims to investigate square ASI donuts using flatspin[8] simulations and Magnetic Force Microscopy (MFM) imaging. The reader will first be introduced to concepts relevant to this work that will shed some light on why these structures are particularly interesting. The different techniques utilized to study the structures are introduced, and the simulated field protocols and physical annealing protocols are mentioned. Lastly, the results acquired are presented and discussed, with a conclusion summarizing what has been done.

Figures are made using Inkscape[9]. Experimental images are processed in Gwyddion[10] and GIMP[11].

Chapter 2

Theory

This chapter gives an introduction to magnetism and summarizes some important concepts to understand when tackling the work conducted in this thesis. It starts by introducing the main building block, the magnet, and its special behavior when the dimensions are reduced to the relevant size. Artificial spin ices and their properties are presented. Lastly, the techniques that were employed are explained. The goal of this section is to give the reader some background knowledge in the theoretical concepts necessary to understand the results obtained in this project.

Relevant sections in this chapter have been reused from the similarly themed project report written in the fall of 2022[1]. The section on magnetism is based on *Magnetism and Magnetic Materials*(2009) by J.M.D. Coey[12].

2.1 Magnetism

Although most people have an intuition about what magnetism is from interacting with everyday objects such as fridge magnets or a compass, the physics behind magnets are quite complicated. Magnetism is a physical phenomenon between moving charges leading to repulsive and/or attractive interactions. The moving charges create magnetic fields around them, which can be described by Gauss' law of magnetism stating that

$$\nabla \cdot \mathbf{B} = 0, \tag{2.1}$$

where **B** is the magnetic field. Since magnetic fields have no divergence, magnetic field lines will have no sources or sinks, and will always have to come in pairs. This is shown for a dipole magnet in figure 2.1.

Although a large magnet with a "north" and "south" pole is perhaps the best known image of magnetism, the basic quantity of magnetism is the much smaller magnetic moment, **m**, which has its origin from electron spin and orbital motion. By averaging the magnetic moments in a solid on a mesoscopic scale in time, we obtain a magnetic moment δm for a given volume δV,

$$\delta m = \mathbf{M}\delta V \tag{2.2}$$

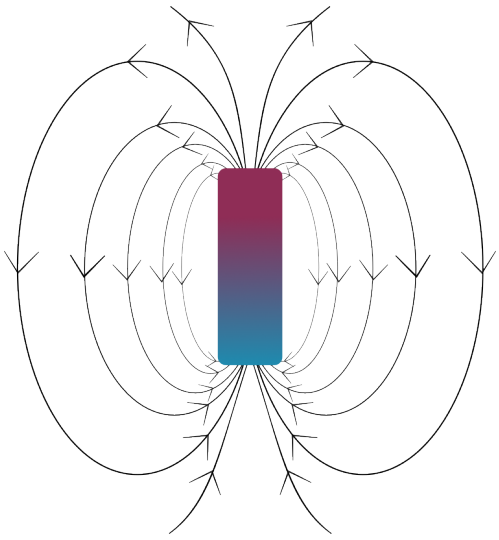

Figure 2.1: A dipole with magnetic field lines going from one pole to the other. All lines have to be connected, because there is no divergence in a magnetic field.

where **M** is the magnetization within the volume. This local magnetization can be averaged over the macroscopic scale by summing over all subregions with volume V_i,

$$\mathbf{M} = \sum_i \mathbf{M}_i V_i \,/\, \sum_i V_i, \tag{2.3}$$

where $\sum_i V_i$ is the volume of the entire sample. The magnetization **M** usually refers to this macroscopic average.

Magnetic interactions can be described through the magnetic field (or magnetic flux density) **B**. However, to avoid having to calculate the complicated local field dynamics inside a sample when it is not necessary, it can sometimes be useful to refer to the magnetizing field **H**. Inside a material, the two fields are related through the magnetization **M**,

$$\mathbf{B} = \mu_0(\mathbf{H} + \mathbf{M}), \tag{2.4}$$

where μ_0 is the vacuum permeability.

Outside a material the magnetization **M** is zero, and therefore $\mathbf{B} = \mu_0\mathbf{H}$. This external field is known as the stray field or the demagnetizing field, and the potential energy contained in the field is known as the magnetostatic energy E_{str}. This energy is given by[13]

$$E_{\text{str}} = -\frac{1}{2}\int \mu_0 \mathbf{H}_d \cdot \mathbf{M} dV, \tag{2.5}$$

where $\mathbf{H}_d$ is the demagnetizing field created by the magnetic body itself, and V is the volume of the body.

If a magnetic dipole is placed in an external field **B**, the potential energy of the dipole becomes

$$E_{\mathrm{m}} = -\mathbf{M} \cdot \mathbf{B}, \tag{2.6}$$

where **M** is the magnetic moment of the dipole. If two dipoles with magetic moments $\mathbf{M}_1$ and $\mathbf{M}_2$ and producing fields $\mathbf{H}_1$ and $\mathbf{H}_2$ are interacting with each other at a separation **r**, their interaction energy is given by[13]

$$E_{\mathrm{dip}} = -\frac{\mu_0}{4\pi|\mathbf{r}|^3}[3(\mathbf{M}_1 \cdot \mathbf{r})(\mathbf{M}_2 \cdot \mathbf{r}) - \mathbf{M}_1\mathbf{M}_2], \tag{2.7}$$

which is known as the dipole-dipole interaction energy.

2.1.1 Magnetic ordering

Materials can have different types of magnetic ordering, depending on which types of energies are dominant. Magnetic ordering can be defined by the magnetic response of the material to an applied field. Diamagnetism, paramagnetism, ferromagnetism and antiferromagnetism are four of the most common types of magnetic ordering. The three latter are shown in figure 2.2

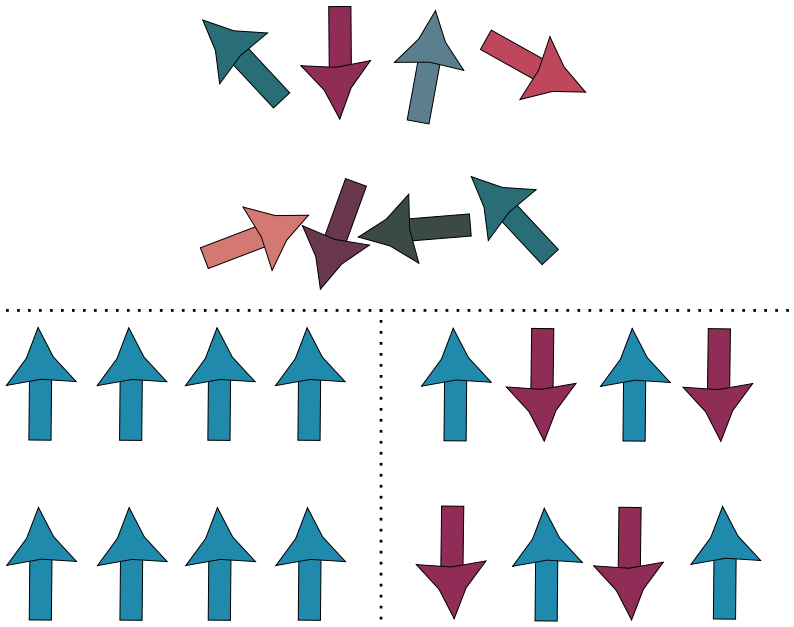

Figure 2.2: Different types of magnetic ordering that can be present in a material. From top to bottom right, the orderings shown are paramagnetism, ferromagnetism and antiferromagnetism.

All materials exhibit a diamagnetic response to some extent, which is the tendency of a material to oppose an external magnetic field, inducing a magnetization in the opposite direction to the field. This effect is weak.

In a paramagnetic state, all atomic magnetic moments sum to zero unless a magnetic field is applied. At zero field, all magnetic moments are randomly aligned, as shown in figure 2.2. Under an applied field, the magnetic moments tend to align with the field, and thus inducing a net magnetization of the material.

Ferromagnets are characterized by an alignment of magnetic moments without the influence of an external field, which leads to a net magnetic moment across the material. This spontaneous magnetic moment happens due to exchange energy from the exchange interaction, which exists between electron spins of neighboring atoms. The energy is given by

$$E_{\text{ex}} = -2\sum_{i>j} J_{\text{ij}}\mathbf{S}_{\text{i}} \cdot \mathbf{S}_{\text{j}},$$

and depending on the sign of the exchange integral J_{ij} results in spins $\mathbf{S}_{\text{i}}$ and $\mathbf{S}_{\text{j}}$ aligning either in a parallel or an anti-parallel fashion. If the alignment is parallel, a ferromagnetic ordering emerges, and if the alignment is anti-parallel, an antiferromagnetic order emerges.

Magnetic anisotropy describes a material's tendency to align its magnetization along a set of preferred directions. The preferred axis or axes are referred to as the easy axes. Anisotropy can arise from crystal structure, material build or shape. These effects are known as magnetocrystalline anisotropy, induced anisotropy, and shape anisotropy. Magnetocrystalline anisotropy arises from the crystal symmetry of a material, while induced anisotropy arises from stress or disordered alloys. Shape anisotropy is present if a material is not perfectly spherical. The magnetization will then align along the longest axis to minimize the demagnetizing field.

Other energy contributions can also lead to specific magnetic ordering, some of the most important being the magnetostatic energy E_{str}, dipole-dipole interaction energy E_{dip}, magnetocrystalline anisotropy energy E_{an} and thermal energy E_{th}. Magnetocrystalline anisotropy energy is the energy contribution needed to switch a magnet away from its easy axis. Thermal energy is given by $E_{\text{th}} = k_{\text{B}}T$, where $k_{\text{B}} = 1.38 \times 10^{-21}\,\text{J}\,\text{K}^{-1}$ is the Boltzmann constant and T is the temperature. The thermal energy can contribute to magnetic ordering in some cases when the temperature is large enough.

The response of a material to an external field can be visualized through a hysteresis loop, where the magnetization of a material is plotted against the applied field. When a field is first applied with increasing strength, the magnetization increases until it reaches the saturation magnetization M_s. Reducing the field will also reduce the magnetization. If the material is ferromagnetic, there will be some remanent magnetization M_r that does not disappear when there is no external field present. When applying a negative field, the magnetization will be reduced even further, equalling zero at the coercivity H_c. When increasing the negative field, the magnetization will again tend towards the saturation magnetization, this time with the opposite sign. A hysteresis loop showing such a behavior is shown in figure 2.3. Based on the shape of the hysteresis loop, a ferromagnet can

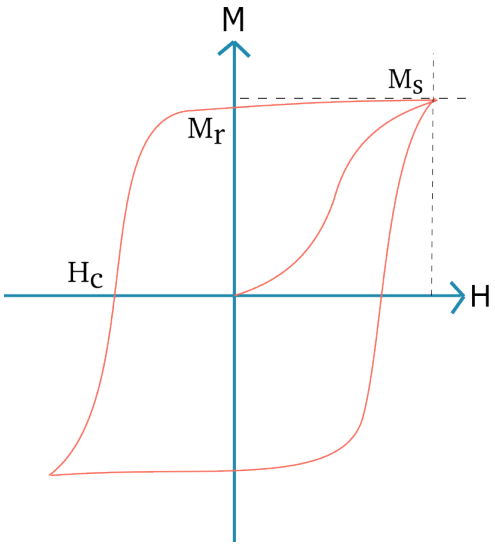

Figure 2.3: Hysteresis curve of a hard ferromagnet. H_c is the coercivity, M_s is the saturation magnetization, and M_r is the remanent magnetization.

either be hard or soft. A hard magnet has a large remanent magnetization when an applied field is removed. A soft magnet has less remanent magnetization, and thus a more narrow hysteresis loop.

2.1.2 Magnetic domains

As all physical systems, magnets want to minimize their energy. To minimize the magnetostatic energy associated with stray fields, ferromagnets tend to form magnetic domains, which are regions within a sample where the local magnetization is saturated[14], meaning that the magnetization is pointing in the same direction across the region. Having multiple regions with different magnetizations means that the overall magnetization of the sample can equal zero, as the regions cancel each other out. When applying a weak field to ferromagnetic materials, the volume of domains aligned with the field will increase, and correspondingly the volume of domains aligned against the field will decrease. If the field is sufficiently strong, all the domains will align with the field, in which case the material only contains one magnetic domain.

The borders between domains are known as domain walls. The formation of domain walls increases the exchange energy at the domain walls, as the magnetic moments on either side of the border are aligned in different directions, which is unfavorable. The formation of domain walls is driven by a trade-off between the minimization of the stray field and the exchange energy. In most cases, it will be more energetically favorable for a permanent magnet to have multiple domains, as shown in figure 2.4, which will lead to an increase in exchange energy and decrease the stray field. However, as the size of the magnet is reduced to nanoscale dimensions, the cost in exchange energy to form domain walls will be larger than

the cost of the magnetostatic energy. Therefore, a nanomagnet prefers to only form a single domain, resulting in a so-called monodomain magnet.

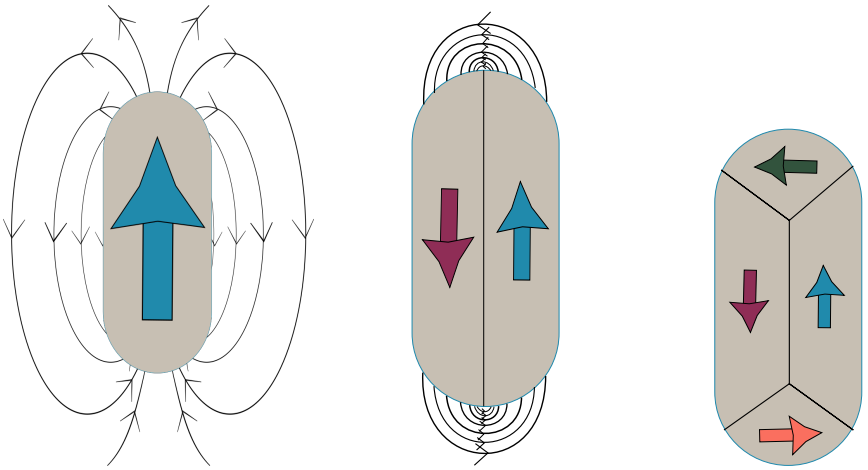

Figure 2.4: The transition from **(a)** a monodomain magnet through **(b)** two domains to a **(c)** multidomain magnet, and how it affects the stray field.

Due to shape anisotropy, a monodomain magnet with one easy axis can be approximated as a dipole, with all of its magnetization pointing in one of the two directions along the easy axis. The magnet can switch between the two directions under the influence of an applied field or temperature. This applied field has to be large enough to overcome the energy barrier created by the anisotropy of the magnet. By increasing the temperature of the system, the switching can happen at lower field values, as an increase in thermal energy makes it easier for magnets to switch. One monodomain magnet with uniaxial shape anisotropy only has two magnetic configurations, but by combining multiple magnets in specific configurations the magnet can be a building block of much more complex materials.

2.2 Artificial spin ice

The following section aims to review the basics of ASIs, while going a bit more in-depth on square ASI and its properties. The content is based on the review *Advances in artificial spin ice* by S.H. Skjærvø et al.(2020)[6].

The term "artificial spin ice" was coined by R.F. Wang et al. in 2006[15], building on the already investigated "spin ice" pyrochlorates. The spins of the spin ice magnetic structures are arranged in such a way that all magnetic interactions cannot be satisfied at the same time[16]. This is analogous to the way that oxygen molecules in water cannot satisfy all their hydrogen bonds simultaneously, and instead end up in a frustrated state[17].

Just like ice, ASIs exhibit local frustration. ASIs are built by combining nanomagnets into periodic and aperiodic structures, forming a larger metamaterial.

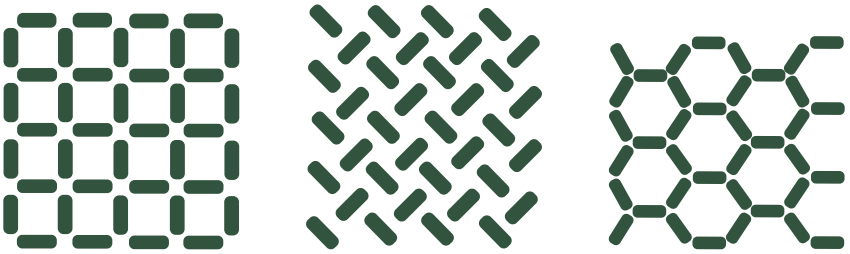

(a) **(b)** **(c)**

Figure 2.5: Three common types of ASI; **(a)** square, **(b)** pinwheel and **(c)** kagome.

A metamaterial is built by combining materials or structures into new materials which retain new emergent properties. In ASIs, these properties arise from the geometric ordering of single magnet building blocks, which prevent them from having all their magnetic interactions satisfied simultaneously.

The building blocks of ASIs are nanoscale ferromagnets. The nanomagnets are elongated along one direction, giving them shape anisotropy and a preferred easy axis that the magnetiation will align with. The shape of the magnets can be varied, as long as there is uniaxial shape anisotropy. The magnets are small enough to be monodomain, and a good model for describing their individual interactions is therefore to approximate them as dipoles with only two possible directions of magnetization along the easy axis. Using equation 2.2 and assuming a ferromagnet with a given volume V and uniform magnetization, the magnitude of total magnetization of each magnet is given by

$$M = M_S V, \tag{2.8}$$

where M_S is the saturation magnetization. The magnitude of magnetization can thus be increased by increasing the volume of the magnets.

Each individual magnet can only have two possible magnetic states. However, since ASIs are designed in such a way that the geometry forces the individual magnets to be frustrated, the overall system will end up in different states depending on which frustrations are dominating under an applied field. The behavior of an ASI can be tuned, based on parameters such as lattice structure, lattice spacing/pitch[1], and size and shape of the individual nanomagnets. There are multiple ways of combining magnets to form ASIs that uphold this geometrical frustration, a few of which are shown in figure 2.5.

2.2.1 Square ASI

Square ASI consists of a lattice made up of multiple squares with one magnet along each side, as seen in figure 2.5a. An $n \times n$ regular square ASI is defined as

[1]Lattice spacing and pitch will be used interchangeably throughout this thesis.

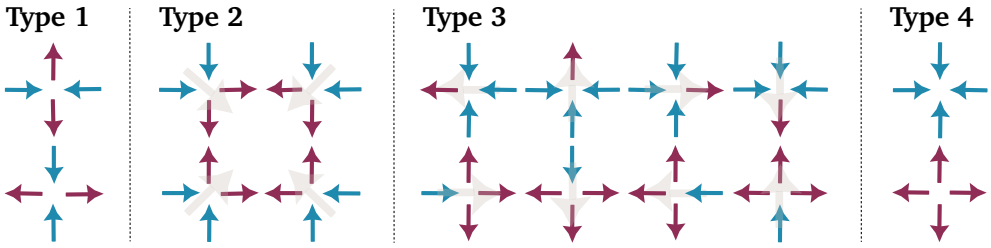

Figure 2.6: Types of vertices that can be present in a square ASI. The weak gray arrows in the background denote the net magnetization of the vertex, if present.

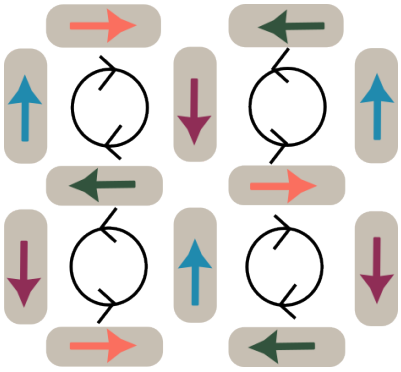

Figure 2.7: Expected ground state configuration for square ASI, illustrated by clockwise and counter-clockwise loops.

having n magnets along each edge of the structure. The closed square ASI contains a total of $2n(n+1)$ magnets including the two extra edges added to enclose all squares in the structure. The points where four magnets meet are called vertices. Due to each magnet having two possible magnetizations, there are a total of 16 possible vertex configurations. These are categorized in four types according to their coupling energy, which are shown in figure 2.6. Type 1 has two magnets with spins pointing inwards, and two pointing outwards. Because this configuration has the lowest energy in a square ASI, it is defined as the ground state, even though the magnets are frustrated. Type 2 vertices also have two spins pointing inwards and two outwards, but additionally a net magnetic moment pointing diagonally across the vertex, which leads to slightly higher energy. Type 3 vertices have three spins pointing inwards and one outwards, or vice versa. The least favorable configurations are type 4 vertices, where all spins are either pointing in or out.

In the ground state, both the sublattice containing horizontal and vertical magnets will have antiferromagnetic ordering. Thus, the entire system is classified as antiferromagnetic. In this state, every second box will circulate in the same direction, both horizontally and vertically. This is shown in figure 2.7. There are two possible degenerate ground state configurations for a square ASI, shifted by one magnet either horizontally or vertically. This degeneracy arises from the antifer-

romagnetic ordering, and can be visualized by flipping all magnets, which will leave the system in an energetically equivalent state. If a square ASI is not fully in one of its two possible ground states, it may have areas with both ground state configurations. The border between these regions would consist of type 2 vertices. Looking at square ASI as having antiferromagnetic ground state ordering, the borders between the two ground state configurations could be characterized as domain walls between two antiferromagnetic domains. Type 3 vertices might also be present, most likely in connection with the domain walls or edges, as the energy of the wall or edge vertices are higher than the ground state type 1 vertices. Type 3 vertices can also appear as separate single-magnet defects in a ground state region. The frustration make it possible to have these domain wall and defect configurations be metastable, and to transition between multiple metastable states by means of external influences. This property makes ASI structures extremely valuable for studying frustration.

Unlike in regular magnetic materials, unfavorable magnetic states can be induced by altering the geometry of ASIs. Such a structure has been investigated by Drisko et al.[18], where they presented a modified square ASI with a lattice edge dislocation. The structure maintained a low energy state across the sample, with the exception of a single domain wall stretching from the defect to the edge. This domain wall would arise from topological frustration due to the dislocation, which in this case means that its presence can be measured far away from the actual defect site[18].

2.2.2 Reservoir computing in ASI

ASIs have many properties that make them beneficial for use in reservoir computing. They have a nonlinear response to magnetic fields, local interactions and rich dynamics, while also being scalable[5]. Fabrication methods are well developed, and there is a large number of reachable states through applying a magnetic field. In a regular $n \times n$ square ASI, there are a maximum of 2^n possible states. The global frustration of the magnets give rise to complex, non-linear behavior, which is ideal for a reservoir. In a reservoir computer, the states of the system are typically represented by the activations of neurons in a neural network[19]. In the case of a reservoir computer that uses ASI as the physical substrate, the states of the system could be represented by the magnetization of the magnets within the material. The more states that can be reached, the more nodes in the reservoir layers. Thus, finding new ways to reach more states are crucial to increase the computing power.

2.3 flatspin

The following section gives an introduction into the ASI simulation tool flatspin. The content is mainly adapted from *flatspin: A large-scale artificial spin ice Simulator* (2020) by J.H. Jensen et al[8].

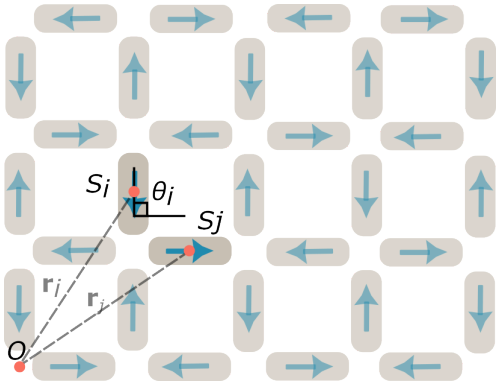

Figure 2.8: In flatspin, each magnet i is represented as a point dipole with a position $\mathbf{r}_i$ defined from the origin O, an angle θ_i given with respect to the horizontal axis, and a spin s_i that takes the value of either 1 or -1, depending on whether the spin is aligned parallel or anti-parallel respectively along the defined angle. The spin parameter is separate from the angle, as this may change during simulations. Figure adapted from J.H. Jensen et al.[8].

flatspin is an ASI simulator enabling simulation of large scale ASIs. Micromagnetic simulation tools would need more computational power than what is practical to capture long-range order and emergent phenomena in large ASI systems. flatspin reduces the computational cost by representing each magnet in the ASI as a point dipole with a given position, angle, and spin. Here, spin refers to the direction of the magnetization in a magnet, and can take the value 1 or -1, depending on whether it aligns parallel or anti-parallel respectively with the defined angle. The angle is given with respect to the horizontal axis, as shown in figure 2.8.

As the magnets in an ASI lattice are approximated as point dipoles in flatspin, it is not possible to vary the size of the magnets to tune the emergent behavior. Instead, a new parameter, α, is introduced to compensate. The dipolar coupling strength, α, is given by

$$\alpha = \frac{\mu_0 M}{4\pi a^3}, \tag{2.9}$$

where a is the lattice spacing , μ_0 is the vacuum permeability, and M is the magnitude of the magnetization. It is possible to tune the pitch directly in flatspin, but the difference between tuning pitch and tuning α is that α also includes the magnetization. The magnetization is related to the volume through equation 2.2, so the physical equivalent to tuning α would be changing lattice spacing and volume of the magnets.

Any magnet i is influenced by up to three external fields

$$\mathbf{h}_i = \mathbf{h}_{\text{dip}}{}^{(i)} + \mathbf{h}_{\text{ext}}{}^{(i)} + \mathbf{h}_{\text{th}}{}^{(i)}, \tag{2.10}$$

where $\mathbf{h}_{\text{dip}}{}^{(i)}$ is the magnetic field stemming from magnetic dipole-dipole interactions, $\mathbf{h}_{\text{ext}}{}^{(i)}$ is an applied external magnetic field, and $\mathbf{h}_{\text{th}}{}^{(i)}$ is a random

magnetic field representing thermal fluctuations.

The dipole interactions are given by[8]

$$\mathbf{h}_{\text{dip}}{}^{(i)} = \alpha \sum_{j \neq i} \frac{3\mathbf{r}_{ij}(\mathbf{m}_j \cdot \mathbf{r}_{ij})}{|\mathbf{r}_{ij}|^5} - \frac{\mathbf{m}_j}{|\mathbf{r}_{ij}|^3}, \tag{2.11}$$

where $\mathbf{r}_{ij} = \mathbf{r}_i - \mathbf{r}_j$ is the distance from spin i to spin j, $\mathbf{m}_j$ is the magnetic moment of magnet j, and α is the coupling strength. The dipole field affecting each spin is determined by summing over the dipole interactions from the spins located in its neighborhood. The size of the neighborhood is adjustable. External fields are modeled as a combination of effective magnetic fields. An applied external field can be set locally for each dipole, globally, or as a vector field varying across the ASI. Thermal interactions can also be modeled, however this was not done in this project and will therefore not be covered here. Further details can be found in *flatspin: A large-scale artificial spin ice simulator*(2020) by J.H. Jensen et al[8].

Defects are always present in physical systems due to fabrication issues, external influences post-fabrication or other contaminations. Simulations are inherently perfect, so to account for the imperfection found in physical systems a small variation in the coercive field of the individual magnets k_{disorder} can be introduced. The variation is obtained from a normal distribution with a standard deviation given by $\sigma = k_{\text{disorder}} \cdot h_k$.

2.3.1 The Stoner-Wohlfarth model and switching

The Stoner-Wohlfarth model considers small ellipsoid-shaped objects that are uniformly magnetized with uniaxial anisotropy and coherent switching under influence of an applied magnetic field[20]. The applied magnetic field can be split up to projections along the easy ($h_\parallel$) and hard axis ($h_\perp$) of the particle. The switching field is then given by the following expression

$$h_{\parallel \text{sw}}{}^{2/3} + h_{\perp \text{sw}}{}^{2/3} = 1, \tag{2.12}$$

plotted in figure 2.9. This plot is known as the switching astroid, and can be used to determine whether switching will occur. If the left side of equation 2.12 is larger than one, meaning that the field is outside of the astroid shown in figure 2.9, the nanomagnet will switch.

The Stoner-Wohlfarth model is only valid for small ellipsoidal magnets, but the model has been generalized by J.H. Jensen et al.[8] to allow asymmetry and differences in the curvature of the magnet extrema. The generalized model is given by

$$\left(\frac{h_\parallel}{b}\right)^{2/\gamma} + \left(\frac{h_\perp}{c}\right)^{2/\beta} = 1, \tag{2.13}$$

where the astroid parameters b, c, β, and γ can be tuned to match the shape and size of the astroid. b and c define the height and width of the astroid, while β

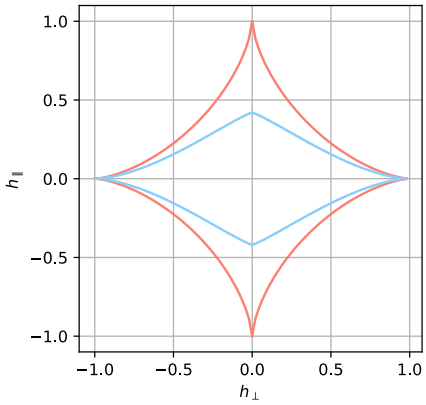

Figure 2.9: The Stoner-Wohlfarth astroid of an ellipsoid (red) and a stadium magnet (blue). The axes correspond to the parallel and perpendicular field with respect to the easy axis of the particle in question. The ellipsoid astroid is obtained by using equation 2.13 with the parameters $b = c = 1$ and $\beta = \gamma = 3$. The stadium astroid is obtained by using equation 2.13 with the parameters $b = 0.42$, $c = 1$, $\beta = 1.7$ and $\gamma = 3.4$. Parameters for stadium magnet obtained from Jensen et al[8].

and γ relate to the curvature of the easy and hard axis respectively. By using the parameters $b = c = 1$ and $\beta = \gamma = 3$, the ellipsoid Stoner-Wohlfarth equation 2.12 is obtained. The astroid for a stadium-shaped particle is obtained by using the parameters $b = 0.42$, $c = 1$, $\beta = 1.7$ and $\gamma = 3.4$[8]. From the switching astroid, it can be seen that unlike for the ellipsoid, a stadium magnet has a smaller switching field when applied along the easy axis than the hard axis. More notably, the switching field is smallest at an angle of approximately $90° \pm 22°$, or $270° \pm 22°$, which means that applying a field at this angle will require the weakest field to switch the magnetization of the magnet.

At each simulation step in flatspin, the total field $\mathbf{h}_i$ of each magnet is calculated. If the Stoner-Wohlfarth criteria is satisfied, magnets will start switching. The magnet with the total field furthest from the switching astroid (figure 2.9) switches first. After every step, the total field for each spin is recalculated, and the process is repeated until there are no more spins that can be flipped. This process assumes a static field during switching, sequential switching, and that the magnet with the highest total field switches first.

2.4 Fabrication techniques

Electron beam lithography (EBL) is a fabrication technique that can be used to fabricate structures of sub-micron size, either by using a positive or negative resist. The resist will change solubility when exposed to an electron beam. Areas around the electron beam spot will also be exposed due to scattering of electrons, limiting

the resolution. A pattern is exposed on the resist-covered substrate using a narrow electron beam, which scans along the sample in a raster-like fashion. After exposure, the sample is developed. If a positive resist is used, the exposed resist will be dissolved, and leave a patterned photoresist layer on the substrate[21].

The entire sample, with patterned photoresist, is then metallized through electron beam evaporation. The photoresist is dissolved, lifting the metal deposited on the remaining photoresist off the sample in a lift-off process. After lift-off, metal remains only on the open areas of the patterned photoresist. However, incomplete lift-off can occur, which would leave photoresist and metal in exposed areas on the sample, and lead to larger conglomerations of metal[21].

2.5 Magnetic force microscopy

The following section on Magnetic Force Microscopy is mainly based on *Introduction to Solid State Physics*(2005) by C. Kittel[14].

Magnetic force microscopy (MFM) is an imaging technique based on atomic force microscopy (AFM), where a vibrating cantilever with a small tip moves across a sample surface in a raster-like fashion, measuring its topography. In AFM, the topography of the sample is measured by exploiting the van der Waals interaction between the tip and the sample. When brought in close vicinity to the sample, the interactions between the sample and the tip will shift the cantilever proportionally to the force, with the proportionality constant being the force constant of the cantilever. The AFM is usually operated in static contact or dynamic non-contact mode. In contact mode, the tip is dragged across the surface of the sample. This may result in damage to the surface structure. Non-contact mode, where the cantilever is oscillating at a distance from the sample, is less invasive than contact mode. To avoid the tip crashing into the sample, a feedback loop adjusts the height of the cantilever in response to the measured change in amplitude by the interferometer.

In contrast to AFM, MFM images the magnetization of the sample. This is done by utilizing a mangetic tip and lifting the cantilever to a certain height above the sample using dynamic non-contact mode. When the tip was in contact with the sample, the van der Waals forces were prominent. These forces scale with r^{-6}, and are therefore only prominent close to the sample. If a sample is magnetic, the dipole interactions between the tip and the sample can be imaged by measuring the phase change of the vibration of the cantilever under the influence of the dipole coupling between the tip and the sample. This coupling scales with r^{-3} (equation 2.7), and will therefore be larger than the van der Waals forces at a distance from the sample. The phase change between the applied and measured vibration is then mapped onto a color scale. In the case of a single monodomain magnet scanned and mapped onto a grayscale, one end of the magnet will be white and one will be black.

A typical MFM setup is shown in figure 2.10. It consists of a piezo stage with a sample holder, so that the sample can be accurately moved in the three spatial

directions x, y and z. Above the sample, a cantilever is connected to an actuator which applies a periodic force to the cantilever, causing it to oscillate. The cantilever position is measured by an interferometer, which uses a laser to measure the deflection of the cantilever.

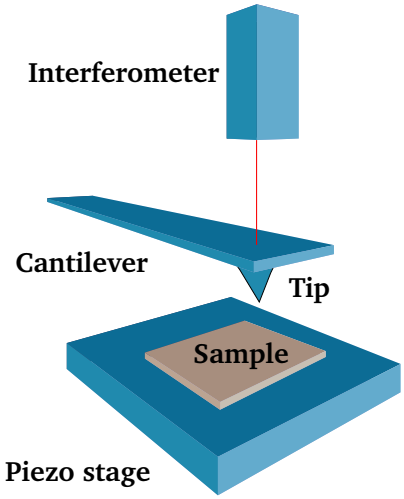

Figure 2.10: Setup of a magnetic force microscope (MFM), including a sample holder with a sample mounted on a piezo stage, a vibrating cantilever with a magnetized tip for MFM, and an interferometer using a laser to measure the position of the cantilever.

Since the MFM tip is interacting with the sample, the tip can in some cases change the magnetization of the sample it is scanning across. This has been done controllably, and utilized to change the magnetization of samples by J.C. Gartside et al[22]. Manipulation of the magnetization was done in AFM contact mode by using a high-moment tip. The method was shown to create topological defects in nanowires and utilized to write specific states in kagome ASIs[23]. Writing does not occur at a tip-sample separation over 5 nm to 10 nm[23], which means that moving it at a lift height higher than this should be safe.

2.5.1 Understanding MFM images

In a square artificial spin ice, the antiferromagnetic ground state ordering will have the weakest contrast. Among the possible orderings in square ASI, this ordering consisting of type 1 vertices has the least frustration between dipoles, and thus the least stray field, which again gives the weakest contrast. The gray low contrast regions will still have a pattern, with slightly darker/brighter contrasts around each end of the individual magnets, as seen in figure 2.11. Discrepancies from this low contrast pattern will indicate a type 2 or 3 vertex. A type 2 vertex indicates a domain wall or multiple magnet defects, and have to appear in connection with edges or other type 2 or 3 vertices. A type 3 vertex can appear either in connection with type 2 vertices, or in pair with another type 3 vertex of

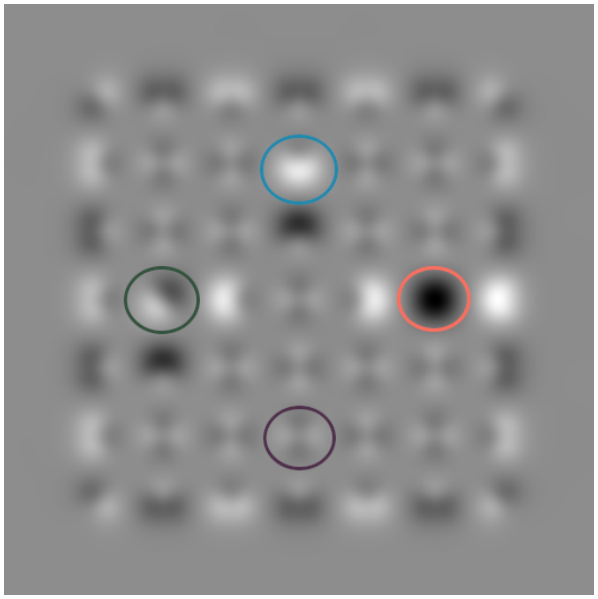

Figure 2.11: A simulated MFM image of a square ASI. The purple circle is a type 1 vertex, the green is type 2, the blue is type 3 and the orange is type 4. Simulated using mumax3[24].

opposite contrast. Two type 3 vertices of opposite contrast indicate that a single magnet has switched magnetization, which is known as a single magnet defect. A change in contrast is expected to be seen along the edges of the donut, where there is one or two less magnets in each vertex. These incomplete vertices will have similar contrast to alternating type 3 vertices, with every other vertex being bright or dark, and with contrast similar to type 2 vertices on the corners. Type 4 vertices are energetically unfavorable, and are therefore highly unlikely to be observed physically in square ASI.

2.6 Annealing ASIs

Forcing an ASI into its ground state can be challenging, but one way of doing it is through annealing. Annealing is the process of heating up a material and then cooling it down, usually with a goal of changing its structure or behavior. The thermal energy reduces the energy barrier needed to switch magnets, and thus makes it easier to relax systems into a ground state. The thicker the magnets in an ASI, the more energy is required to flip the magnets, and thus the higher temperature is needed to reach a ground state[25].

Chapter 3

Methods

3.1 Design of modified donut structure

Two ASI structures were investigated in this project; a "donut" and a "modified donut". The basis of the structures is an $n \times n$ regular square ASI comprised of stadium-shaped magnets with lateral dimensions of 220×80 nm. The donut was constructed by removing a $k \times k$ (where $k = a/3$) square ASI from the center of the $n \times n$ square ASI, creating a square hole in the center of the original ASI and ending up with a square annulus-like structure, as shown in figure 3.1a.

To make the modified donuts, a structural lattice defect was introduced by removing one column of vertical and horizontal magnets from the top central square of the donut. The magnets left in the top square were then shifted horizontally to keep an even horizontal lattice spacing throughout the region. An example of a modified donut is shown in figure 3.1b, with the modified lattice spacings shown in table 3.1. This design was originally developed during the project report work in the fall of 2022[1].

The geometry of the modified donut makes it impossible to have a uniform ground state without a domain wall present, as shown by Drisko et al[18]. Theoretically, if there are multiple domain walls crossing from the inner square to the outer rim, these have to appear in an odd number. This "parity rule" also holds

	Top square pitch [nm]		Top square nearest spacing [nm]	
Regular donut	295	305	30	37
12×12	393.3	406.7	68.5	76.8
24×24	337.1	348.6	45.4	53.0
36×36	321.8	332.7	39.5	46.9
72×72	307.8	318.3	34.2	41.5
108×108	303.4	313.7	32.6	39.8

Table 3.1: Horizontal pitch and nearest neighbor distance in the modified region in modified donuts for given sizes and regular lattice spacings.

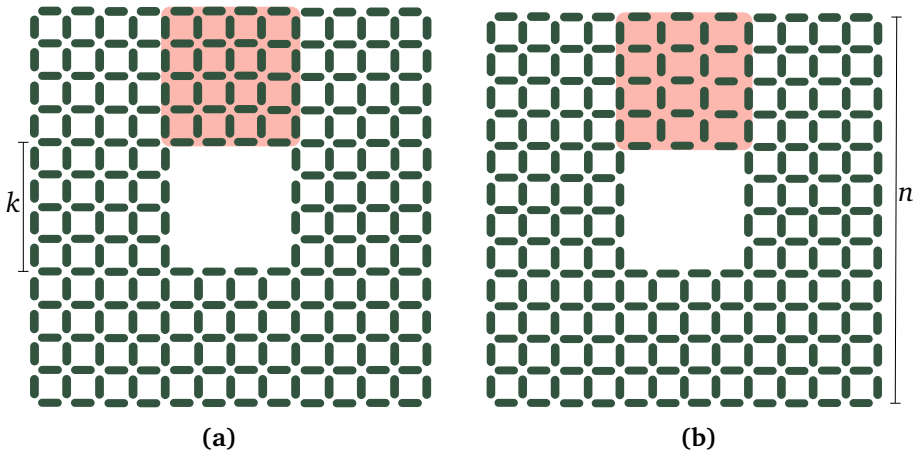

Figure 3.1: (a) A square ASI regular donut and **(b)** a square ASI modified donut. The modified region is highlighted in both structures. The size of the structures n and an introduced size adjustment factor $k = n/3$ are shown. For this specific structure, $n = 12$ and $k = 4$.

for the structure without the lattice defect, where the number of domain walls always has to be an even number. A possible ground state of the defect region of the structure is shown in figure 3.2.

But how can there be one domain wall and only one domain at the same time - when a domain wall per definition is a wall between *two* domains? Or equally, how can there be two different domains on either side of the domain wall, when the domains that look to be different at the domain wall at the same time are connected and part of the same domain everywhere else? To better understand this, one can consider a Möbius strip[18]. If each length unit of the strip is represented by a vector with a direction perpendicular to the strip surface, the local variation between vectors will be minimal. However, at one point of the strip two vectors pointing the exact opposite way will be adjacent to each other. In the same way, a square ASI structure with a topological defect can be in one antiferromagnetic ground state ordering throughout, except for one domain wall.

3.2 Simulations

flatspin[8] simulations were performed to gain an understanding of the effect of an applied magnetic field on modified donuts. Simulations were performed on three systems; a rectangular 24×8 square ASI, a 24×24 regular donut, and a 24×24 modified donut. Donut simulations with high αs were done using the NTNU computing cluster IDUN[26].

The donuts were made using the `CustomSpinIce` class, with the `SquareSpinIce` class as a basis for the positions and angles. In the modified donut, the lattice spacing of the top square was modified to include one column less of horizontal

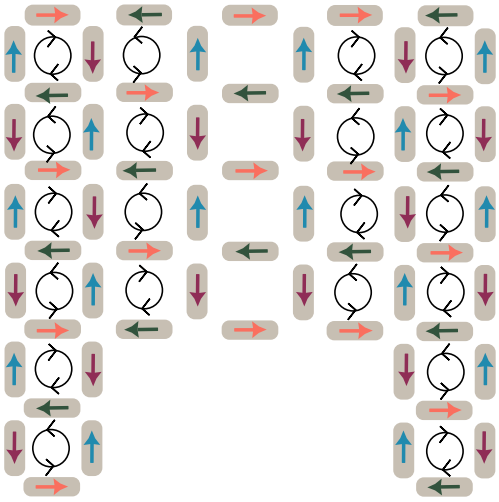

Figure 3.2: The top region of a modified donut with a topological defect causing an interruption in the antiferromagnetic ordering of clockwise and counterclockwise loops.

and vertical magnets while still keeping an even lattice spacing throughout the region.

An adjustable factor $k = n/3$ was included so that the size of the structure could be easily adjusted. k corresponds to the number of magnets along the edges of the inner square hole. The resulting geometry was exported as two files, one containing position and one containing angles, which were used to create the mask used in patterning the physical sample. These files were made during the project report work done in the fall of 2022[1].

The magnetic configuration of the modified donut is expected to contain at least one domain wall, as shown in figure 3.2. Thus, the ground state of this structure is initialized with one domain wall. Ideal placements of this domain wall is determined through simulations.

The goal of the simulations is to look into the behavior of domain walls in donuts under the influence of an applied field. This is done by initializing both structures with either one or two domain walls, and applying field protocols.

3.2.1 Triangular field protocol

To facilitate switching of the magnets in the square ASI structure, a flatspin encoder called `AngleTriangle` was utilized[8]. This encodes the input field as the angle of a triangle wave global field. The encoder has a constant field magnitude H, and scales between two defined angles ϕ_0 and ϕ. A timestep parameter decides the number of repetitions of the applied field. In this work, the encoder was given angle input corresponding to $\pm$ 22° degrees of a given angle θ. These specific angles are chosen to minimize the field needed to switch the magnet, according to its Stoner-Wohlfarth astroid, shown in figure 2.9. θ+22° will either correspond

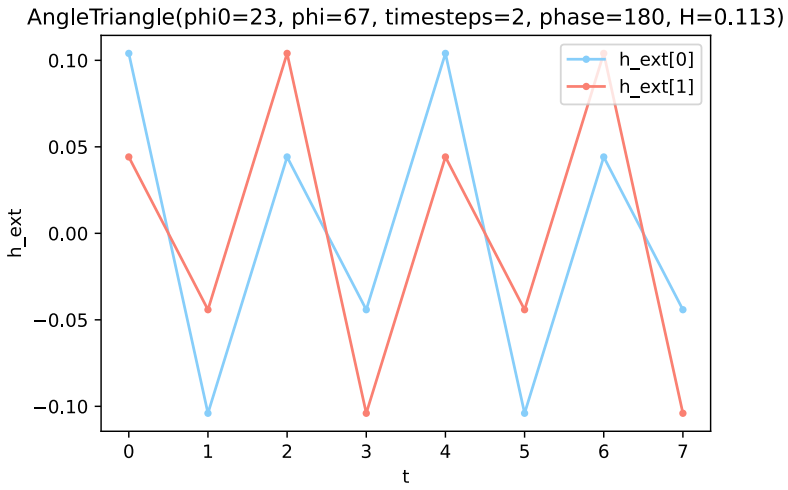

Figure 3.3: A triangular field protocol applied at a 45° ± 22° angle with two timesteps and a maximum field strength of 113 mT.

to a vertical or horizontal magnets' easiest switching axis, and $\theta-22°$ will correspond to the differently oriented magnets' easiest switching axis. This "triangular field protocol" is shown in figure 3.3 for a field of 113 mT and an angle of 45° ± 22°.

3.2.2 Visualization

The standard flatspin plot shows all the magnets as color-coded arrows pointing along the direction of the magnetization. Antiferromagnetic systems are difficult to visualize using only this technique, as the images look very chaotic. Usually this is solved by plotting the magnetization of vertices. Vertices are found using grids defined on the structure. In the modified donuts this is problematic, as the lattice spacing in the modified region is not equal to the rest of the structure. One possible plotting technique that does not rely on even lattice spacing is visualization based on photoemission electron spectroscopy, where the magnitude of magnetization of each magnet in a certain direction (here: 45°) is plotted on a greyscale with vectors indicating the direction. This technique works well for curved domain walls, but straight domain walls can be challenging to spot. Voronoi plots plot the magnets as a vector pointing in the direction of magnetization, like the two other techniques. In addition, the dipolar fields from neighboring magnets are plotted using the backround of the region closest to each magnet. Different colors correspond to different directions of the field, and intensity corresponds to magnitude of the field. Voronoi plotting is not a linearly dependent operation, and will therefore not fail in the region with the adjusted lattice spacing. The three visualization techniques are shown in figure 3.4. Voronoi plots are used going forward, as they clearly highlight domain walls when they are both regularly and

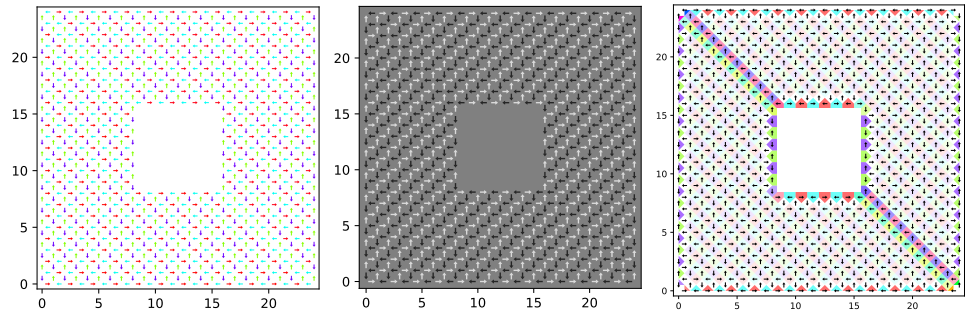

Figure 3.4: A 24×24 donut with two diagonal domain walls visualized using different methods. In **(a)**, the standard flatspin format plotting each magnet as an arrow in one of four different colors corresponding to the direction of magnetization. **(b)** uses a photoemission electron microscopy (PEEM) inspired visualization. **(c)** uses a voronoi plot depicting the dipole field of the surrounding magnets.

irregularly shaped.

3.2.3 Determining the critical field

A critical field H_{cr} is defined through simulations for a given structure, size, angle and α. First, a region of interest of field values is found by determining the field strength needed for the first magnet to flip, and the field strength needed to polarize the structure. Then, simulations are run for this region in increments of 1 mT. The field value where magnets that are not connected to the domain wall or at the edges start to flip is the critical field value H_{cr}.

3.2.4 Preliminary simulations

Preliminary simulations were performed to determine which α would result in the most movement of the domain walls before the magnets in the ground state domain(s) started to switch. Simulations were run on a rectangle made up of a regular square spin ice initialized with one domain wall and αs stretching from 0.0005 to 0.003 in increments of 0.0005, plus an additional first alpha of 0.0001. A field protocol with a triangular field switching back and forth between $45° \pm 22°$ was applied to the structure. For each simulation, the critical field was determined. All simulations are shown in appendix 2.

3.3 Sample fabrication

The sample used for most results presented in this thesis is hereafter known as sample B. Its design was made by Ida Breivik using position and angle data from the performed flatspin simulations. The physical samples were fabricated at NTNU NanoLab by Ida Breivik using an Electron Beam Lithography process, as described

in section 2.4. The magnets were fabricated in permalloy on top of a silicon substrate. The stadium-shaped magnets were $220 \times 80 \times 25$ nm.

20 different structures were fabricated on sample *B*, ten regular and ten modified donuts, of sizes 12×12, 24×24, 36×36, 72×72 and 104×104, with a pitch of 295 and 305 nm. This corresponds to the closest spacing between the nearest neighbor magnets being 29.6 nm and 36.7 nm respectively.

Another sample with slightly different sample design was made by Anders Strømberg for the project report work done during the fall of 2022[1]. These samples were exposed in the fall of 2022. One of the remaining samples was metallized in January of 2023 to be used in this project. The sample, hereby known as sample *A*, was fabricated using a similar procedure to sample *B*, except for the different sample design and structures included, and that the size of the magnets was $220 \times 80 \times 10$ nm.

3.4 Magnetic force microscopy

3.4.1 Image acquisition

Two samples were studied using MFM. All MFM measurements were performed at room temperature. Each sample was glued to a sample holder with electrical contacts using silver glue, to ground the sample. When the sample was mounted in the MFM, the structures had to be found. An approximate position of the sample was found by moving the piezo stage so that the alignment marks pointing out the structures on the sample lined up underneath the cantilever. The exact position was found by imaging an area and analyzing the structures found in the area. To find structures within the field of view of the microscope, two techniques were employed; either, MFM scans with low resolution and fast scan speeds were used, or the tip was dragged across the field of view in contact AFM mode in different directions, while the live feedback loop was being used to determine where the structures are.

A selection tool was used to select the size and placement of the scan region. The scan speed decides how fast the cantilever moves across the sample, and is set for each scan. In MFM mode, the tip is not in contact with the sample, and can therefore be set at a high speed, especially for high lift heights. In AFM contact mode, the tip operates close to the sample, and must therefore be set to a lower speed than in non-contact mode to avoid the tip crashing into the sample. Speeds of $1\,\mu m\,s^{-1}$ to $2\,\mu m\,s^{-1}$ were utilized in this project.

After the desired sample area was found, preliminary scans with a high lift height and low resolution were performed to scout for possible defects and to determine what a safe lift height would be. This was usually done at about 120 nm to 180 nm lift height with a speed of $10\,\mu m\,s^{-1}$ to $12\,\mu m\,s^{-1}$, and a resolution of 150×150 pixels. When the proper imaging area was chosen, the selected area was slope compensated. Final scans were performed at a lift height of 60 nm to 120 nm, depending on what was determined to be safe, with a resolution of 400×400

pixels and a speed of $6\,\mu m\,s^{-1}$ to $10\,\mu m\,s^{-1}$.

Multiple steps were taken to maximize contrast and quality of acquired MFM images. A bias was applied to adjust the optical path distance from the cantilever to the interferometer so that any change in the cantilever height would induce the largest possible change in the measured interferometric distance. This was done through dithering, by analyzing the change in amplitude depending on the applied bias. The working point was set to the steepest point, which corresponds to one of the midpoints on the sinusoidal-like curve. In addition, the cantilever excitation frequency was adjusted to be as close as possible to the resonance frequency of the cantilever, giving a higher amplitude for the applied excitation voltage. A z-axis spectroscopy scan was performed to find the exact moment the tip is brought into contact with the sample. To avoid crashing into the sample, the working point was set to 80% of the amplitude of the cantilever when it is not in contact with the sample.

3.4.2 Image processing

Gwyddion[10] was used to process the raw images when needed. Uneven backgrounds were removed by mean plane subtraction, and the rows were aligned using either a median or linear fit method, depending on what gave the best alignment. GIMP[11] was used to crop and rotate images, and to highlight or mark specific areas.

3.4.3 Quantization of data

To extract quantized data from the images, features were counted so they could be plotted against each other. Four main types of feature were counted: Domain walls stretching from the hole in the middle to the outer edge, domain walls that either bite their own tails and form a loop or start and end at the edges, magnet defects in the modified region, and magnet defects in the entire structure. Magnet defects are type 2 or 3 vertices not connected to a domain wall, or type 3 vertices connected to a domain wall. This definition is used so that domain walls, which consist mainly of type 2 vertices, can be counted separately. If there are multiple type 2 vertices close to each other, but no ground state region between them, they are counted as magnet defects.

3.5 Annealing procedure

An annealing protocol was performed to relax the investigated ASI structure. The sample was removed from the sample holder and put on a hot plate. The hot plate was heated to 300°C, and kept at that temperature for 4 minutes. After annealing, the sample was removed and put on a room tempered metal slab to cool. When the sample reaches room temperature, it was mounted back on the sample holder and reinstated in the MFM. Initial imaging after annealing showed minimal change, so

the sample was dismounted again and annealed at 400°C for 5 minutes, followed by cooling on the tempered metal slab.

Chapter 4

Results and discussion

4.1 Preliminary simulations

Preliminary simulations were performed on a rectangular 24×8 square ASI, to determine the ideal working αs for maximum domain wall movement.

An initial disorder of 5% was tested for square ASI simulations. For small systems, the presence of disorder made it difficult to know whether the domain wall had been moved, or whether random disorder switching was the cause of magnets close to the domain wall switching. Simulations were therefore performed with 0% disorder for the results presented in this thesis.

4.1.1 Initializing the domain wall

The three simulated systems, a 24×8 square ASI, a regular donut and a modified donut, were initialized to contain one (square ASI and modified donut) or two (regular donut) domain walls. In the square ASI, the domain wall was initialized vertically between the 11th and 12th magnet, as seen in figure 4.1a. The initial domain wall was made up of type 3 vertices.

A field was then applied to an initialized square ASI with $\alpha = 0.002$. The field was applied using the triangular field protocol at $135° \pm 22°$, and increasing the field by 1 mT for every simulation run. At 69 mT, single magnets close to the domain wall started to switch. At 73 mT, the domain wall shifted to the state shown in figure 4.1b, where the domain wall now consisted of only type 2 vertices. At 90 mT, central magnets started to switch. Excluding the edge magnets, the shape of the domain wall was still the same as the one shown to the right in figure 4.1b until central magnets started to switch. Similar procedures were performed along both diagonals in both directions, namely $45° \pm 22°$, $225° \pm 22°$ and $315° \pm 22°$, all showing a similar slight initial movement of the domain wall relaxing into a type 2 domain wall.

The goal of the simulations were to move the domain wall away from its relaxed state. As the domain wall relaxed away from the first initialized state, the new type 2 domain wall configuration shown in figure 4.1b was used going for-

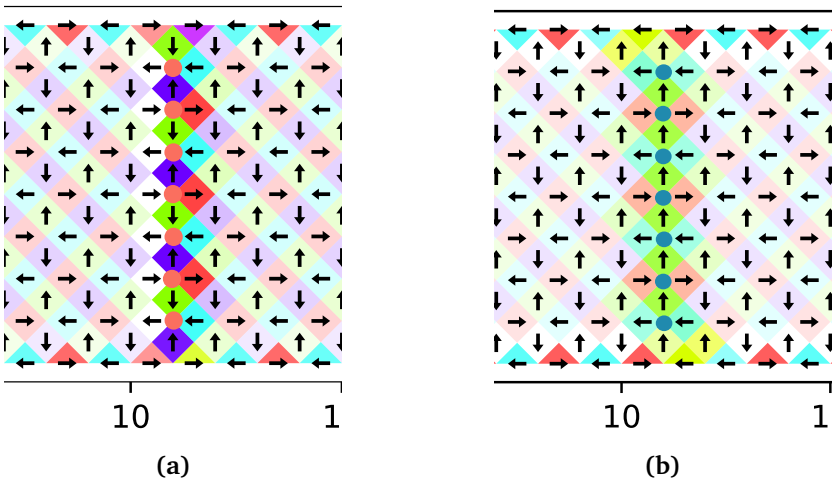

Figure 4.1: (a) The first initialized domain wall in a sqare ASI, consisting of type 3 vertices marked with orange circles. **(b)** The domain wall after a field of 79 mT has been applied at at 45° ± 22°, consisting of type 2 vertices marked with blue circles.

ward as the initial state, so that any deviation can be assumed to correspond to an increase in frustration. Type 2 vertices have lower energy than type 3 vertices, and so the observed relaxation into this configuration is expected. A type 2 initial ground state configuration was also used for simulating donuts, due to the relaxed type 2 domain walls found in the preliminary simulations.

4.1.2 Coupling constant (α)

Preliminary simulations that were performed on a 24×8 square ASI to determine the ideal working α are presented in figure 4.2. Movement of the domain wall was measured relative to the expected ground state shown in figure 4.1b. Movement was quantized by counting the horizontal distance in magnets at two points; from the flipped spin furthest away from the initialized domain wall that was still connected to the domain wall, and from the place the domain wall crossed the middle row of the structure. A schematic representation of the movement measurement is shown in figure 4.2b.

Simulations were performed using a 45° ± 22° triangular field protocol. For each α, a run of simulations were performed. The critical field value for the simulated αs are shown in table 4.1. The movement of the domain wall was defined as the amount of movement present after applying field values just below this critical value.

From the results presented in figure 4.2, it seems like a larger α will lead to more movement of the domain wall under the influence of an applied magnetic field. However, this comes at a large energetic cost, as a higher α requires a higher applied field to switch magnets.

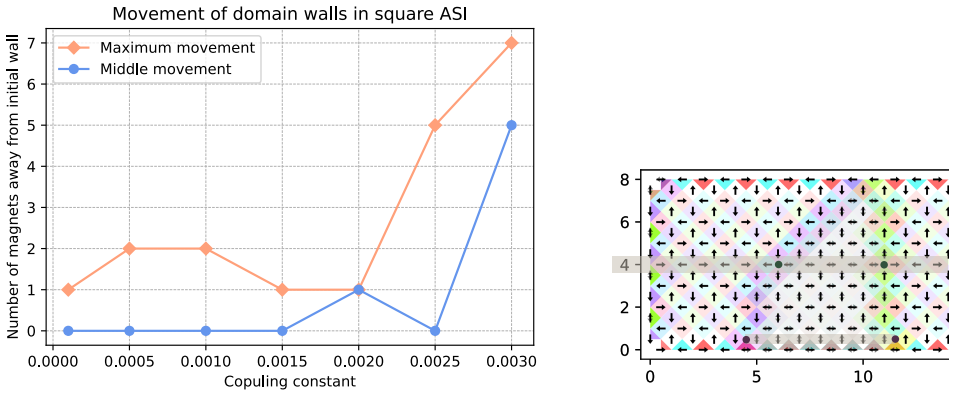

(a) **(b)**

Figure 4.2: (a) Amount of shifting of a domain wall depending on the coupling parameter α. **(b)** shows how the two movements of the domain wall is measured, by overlaying an image of a moved domain wall over the initial wall. The maximum movement is the number of magnets between the flipped magnet furthest away from the domain wall that is still connected to the wall, and the initialized domain wall. Middle movement is the number of magnets from the place where the domain wall crosses row 4 to the initialized domain wall. Simulations were performed on a 24×8 magnet regular square ASI, and the applied field was 113 mT following a triangular field protocol applied in the $45^\circ \pm 22^\circ$ direction.

Coupling constant	Critical field [mT]
0.0001	77
0.0005	80
0.001	83
0.0015	96
0.002	103
0.0025	106
0.003	114

Table 4.1: Critical field H_{cr} for a 24×8 square ASI with different coupling constants.

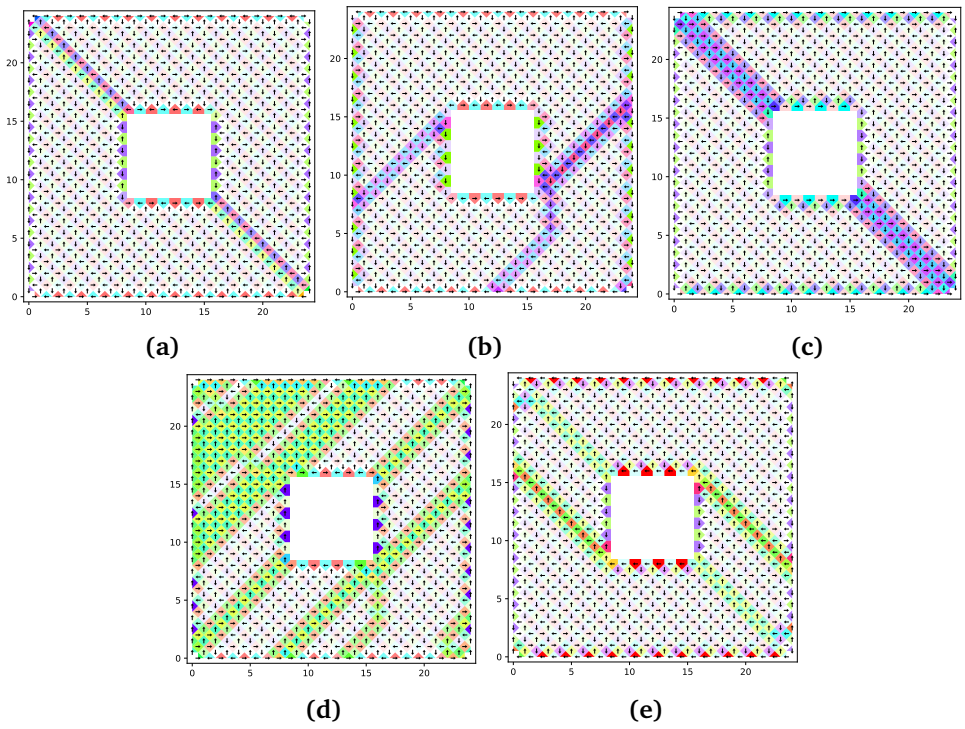

Figure 4.3: (a) A 24 × 24 donut initialized with two domain walls along the 45° diagonal. **(b)** The initialized donut after an applied field of 113 mT applied at a 45° ± 22° angle. **(c)** The initialized donut after an applied field of 113 mT applied at a 135° ± 22° angle. **(d)** The initialized donut after an applied field of 113 mT applied at a 225° ± 22° angle. **(e)** The initialized donut after an applied field of 113 mT applied at a 315° ± 22° angle.

4.2 Donut simulations

The critical field value H_{cr} of a 24×24 regular donut with $\alpha = 0.003$ was determined to be 113 mT from similar simulations as in section 3.2.3. A 113 mT field was applied along both diagonals and in both directions, namely 45° ± 22°, 135° ± 22°, 225° ± 22° and 315° ± 22°. The initial domain wall aligned along the 135° or 325° diagonal is shown in figure 4.3a. When applying the triangular field protocol in the 45° ± 22° direction, the domain walls flipped 90° and aligned with the 45° diagonal, as seen in figure 4.3b. When a field was applied in the 315° ± 22° direction, the domain walls observed aligned with the 315° diagonal, as seen in figure 4.3e. Similar diagonal alignment were seen for the 135° ± 22° and 225° ± 22° field directions as seen in figure 4.3c and 4.3d. It seems like domain walls tend to align in the direction of the applied field.

Similar simulations were performed on the modified donut, with the domain wall initialized along the lower right diagonal as seen in figure 4.4a, but the large lattice spacing in the modified region made moving the domain wall more difficult. As the critical magnetic field H_{cr} value where magnets started to switch was

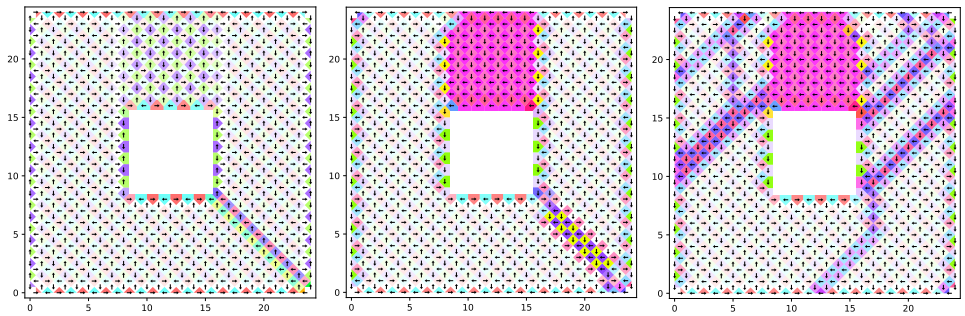

(a) **(b)** **(c)**

Figure 4.4: (a) A 24×24 modified donut, initialized with one domain wall along one side of one of the diagonals. **(b)** The initialized donut after an applied field of 112 mT applied at a $45^\circ \pm 22^\circ$ angle. **(c)** The initialized donut after an applied field of 113 mT applied at a $45^\circ \pm 22^\circ$ angle.

much lower in the region with larger lattice spacing, the domain wall was slightly widened, but did not move before the critical value of 102 mT was reached. The shape of the domain wall stayed the same until the entire modified region was polarized, which can be seen in figure 4.4b. When increasing the field further, the domain wall would shift. A new critical value $H_{\text{cr-mod}}$ was defined as the value when magnets outside the region with larger lattice spacing started to switch. This new critical value of 113 mT equals the critical value of the same size regular donut having the same α. Applying the higher critical field $H_{\text{cr-mod}}$ needed to move domain walls in the regularly spaced region polarized the modified region, making it impossible to track domain wall movement in this region. Going forward, the critical field value will refer to H_{cr} for regular donuts, and $H_{\text{cr-mod}}$ for modified donuts.

The creation of new domains was seen close to the critical value for both the regular donut (figure 4.3) and the modified donut (figure 4.4). This is interesting, as inducing domain walls in a structure could be another way to reach more magnetic states. However, multiple domain walls appearing at a single 1 mT increment makes it challenging to design a protocol to controllably set magnetic states.

An α as high as 0.003 is not physically realizable due to limitations in fabrication. It is possible that the domain wall creation happens because of the artificially high α. As mentioned, high α leads to more switching before the critical field is reached. If so, this behavior is unlikely to appear in physical systems unless fabrication techniques improve, making it possible to realize higher αs.

Multiple field protocols were tested, listed in appendix 2. Although some of the simulation protocols shifted the domains and the domain walls, and even created new ones, it proved difficult to control the movement through a specific protocol. In the future it would be helpful to simulate on larger systems with some introduced disorder, and with a physically realizable α.

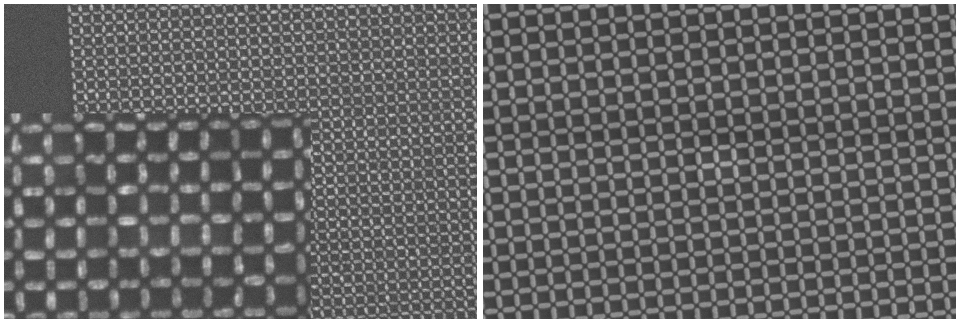

(a) **(b)**

Figure 4.5: SEM images of 108 × 108 donut structures. **(a)** Donut from sample *A* with a pitch of 325 nm. Infield is a zoomed in image of the same structure. **(b)** Donut from sample *B* with a pitch of 305 nm.

4.3 SEM imaging

Two samples, sample *A* and sample *B*, were investigated, mainly using MFM. Scanning Electron Microscopy (SEM) images were acquired after fabrication. There are significant differences between the single magnets in the two ASI structures, as seen in figure 4.5. Figure 4.5a show differences in contrast across each magnet, while the magnets in figure 4.5b are more uniform.

The irregularities seen in sample *A* were also seen in SEM images of the samples metallized for the project report work in October 2022[1]. The uneven intensity across the magnets suggests a difference in height or composition of the magnets. As all samples exposed and developed in the same batch showed the same types of irregularities, it seems likely that the irregularities appeared before the metallization step. As sample *A* was exposed and developed as part of the sample batch created for the project report in October 2022[1], the resist was quite old when metallization and lift-off was performed in January 2023. It is possible that there were remaining pieces of resist left in the exposed areas after exposure. If so, the permalloy would get deposited unevenly on top of this. Dust could possibly have contaminated the surface, or it is possible that something happened during metallization. The samples from the first batch were metallized at different times, and thus it seems unlikely that the same metallization contaminations would affect both samples. After metallization, the sample could have been oxidized. Oxidation takes some time, and because of the relatively short time frame between metallization and preliminary imaging, this seems unlikely too.

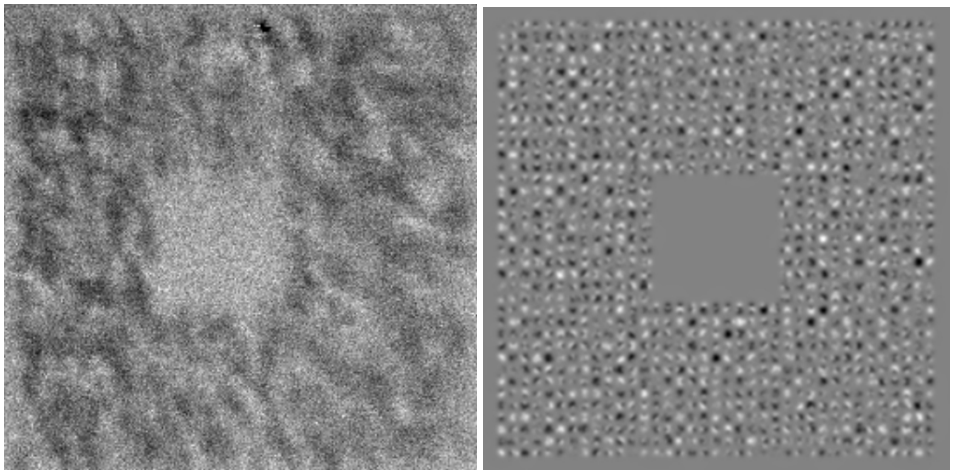

(a) **(b)**

Figure 4.6: (a) MFM image of a 36 × 36 modified donut from sample *A*. **(b)** Simulated MFM image of a 36 × 36 regular donut with random magnetization in all magnets. Simulated using mumax3[24].

4.4 MFM imaging

4.4.1 Sample *A*

The sample was analyzed using MFM, but the resulting images showed diffuse contrasts across the sample, as shown in figure 4.6a. The contrast is not periodic enough to suggest a ground or polarized state. The seemingly random dispersion of weak magnetizations suggest that the magnets are highly irregular, and thus exhibit no uniform magnetic state. The obtained image is compared with a simulated MFM image with random magnetization, leading to magnets no longer being single-domain, shown in figure 4.6b. The images shows a similar type of ordering, which might suggest that the magnets are not monodomain.

To investigate this further, height profiles were extracted from AFM images of the structures. These are shown in figure 4.7. The irregular height profile of sample *A* could explain the random magnetization, as height difference in itself would give variations in contrast due to the dipolar coupling scaling with r^3 and thus being weaker when the tip is further away from the sample. It is also possible that the loss of uniformity would make the small magnets form multiple magnetic domains both within and out of the xy plane, as the samples are no longer purely uniaxial. As the height of the magnets in sample *A* is comparable to sample *B*, it is likely that most of the magnetization will still be pointing along the easy axis. Because of the coarse structure on the surface, it is however possible that there are small local variations in magnetization. Depending on the origin of the irregularities, the permalloy could be strained. All of these things would lead to changes in the local magnetization, and thus change the dipole-dipole interactions between the sample and the tip.

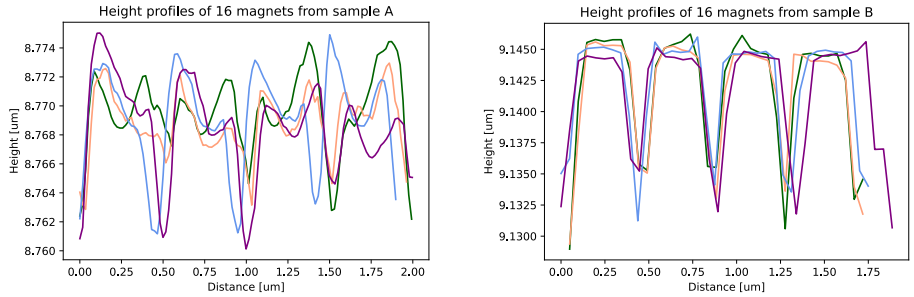

(a) **(b)**

Figure 4.7: Height profiles across different magnets from **(a)** sample *A* and **(b)** sample *B*. Acquired using AFM.

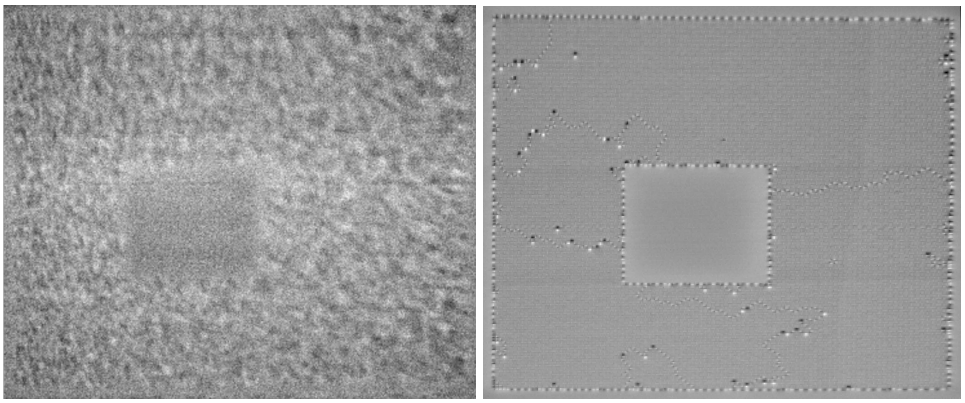

(a) **(b)**

Figure 4.8: MFM image of a 108 × 108 donut with a pitch of 295 nm **(a)** from sample *A* and **(b)** from sample *B*.

As the magnets were showing such highly irregular behavior, sample *A* could not be used for analysis of domains. A second batch of samples were fabricated, and these looked much more promising. Sample *B* from the second batch was used for all the following analysis.

4.4.2 Sample *B*

Sample *B* was fabricated to replace the irregular sample *A*. There was an immediate difference in magnetic contrast between the two samples, as shown in figure 4.8. Where sample *A* appeared to have random magnetization, sample *B* had mostly ground state ordering, with some domain walls and defects breaking up the ordering. Preliminary flatspin simulations presented in figure 4.2 showed that a higher α would be beneficial for the movement of domain walls, and so the samples were made to be thicker than the previous batch (25 nm compared to the previous 10 nm) to increase α. Using equations 2.8 and 2.9, and an M_S

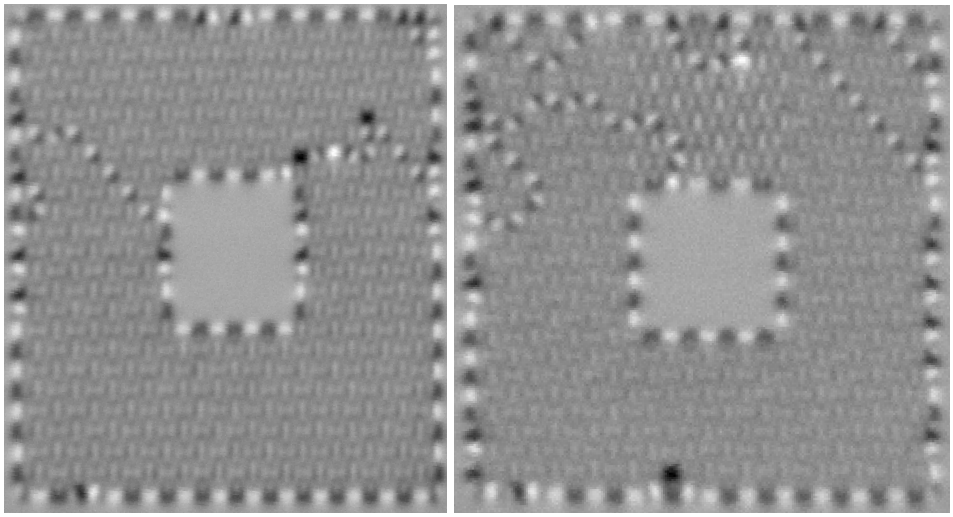

(a) **(b)**

Figure 4.9: Acquired MFM images of the 24×24 **(a)** regular donut and **(b)** modified donut, both with a pitch of 295 nm.

of 860×10^3 A/m for permalloy, this corresponds to an estimated α of 0.00147 for the donuts with lattice spacing of 295 nm, and 0.00133 for the donuts with lattice spacing 305 nm. Adjusting for physical impurities such as the magnets not being dipoles based on experiences in the research group, α can be estimated to be 0.0023 for the donuts with lattice spacing of 295 nm, and 0.0021 for the donuts with lattice spacing 305 nm. Both of these estimations are significantly lower than the simulated alpha of 0.003. α will be even smaller for the modified regions with increased lattice spacing.

The sample consists of twenty structures, half being regular donuts and half being modified donuts. In figure 4.9, two donuts with the same size (24×24 magnets) and lattice spacing (295 nm) are shown. The only difference is the modified region. The change in lattice spacing in this region can be seen in the change of contrast in the upper central region in image 4.9b. The modified region has more contrast due to the dipole-dipole energy between the magnets and the tip being stronger when the magnets are further apart. A larger distance leads to less frustration between the stray fields of the magnets, and thus a larger stray field, which in turn will lead to stronger dipole-dipole interactions between the tip and the sample and give more contrast.

When acquiring MFM images, sample B required slightly higher slope compensation than sample A in the x direction. Along the y axis, the slope compensation had flipped. Where negative compensation was needed for sample A, it was necessary to use positive compensation for sample B. This change in slope could be because old silver glue residue from the former sample was not removed properly before attaching the new sample.

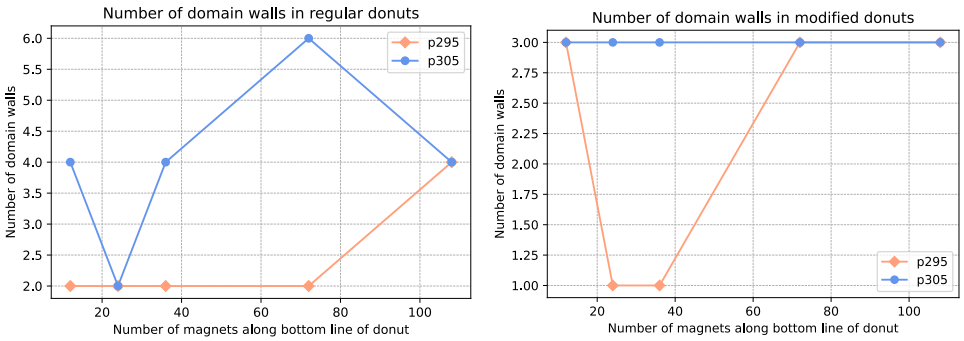

(a) **(b)**

Figure 4.10: Number of domain walls stretching from the central hole to the edges in different sized **(a)** regular donuts and **(b)** modified donuts, with two different lattice spacings, 295 nm and 305 nm. Note that the number of domain walls is always even for regular donuts and odd for modified donuts. Counted from MFM images, all of which are shown in appendix 1.

4.4.3 Domains and domain walls

There are multiple domains in all structures imaged in this work. The lack of ground state order can come from a multitude of things, including external fields from surroundings, contaminations, defects, physical shape variations of the magnets or temperature influences.

Figure 4.10 shows the number of domain walls stretching from the inner square to the outer rim in each structure. The number of domain walls was predicted to always be an even number for the regular donuts and an odd number for the modified donuts, which is also seen in figure 4.10. Structures with larger lattice spacing seem to form more domain walls than structures with smaller lattice spacing.

Figure 4.11 shows the simulated and the experimental image of a 12×12 regular donut. The ground state ordering can be seen throughout most of the image, with two domain walls and some single-magnet defects along the edges or connected to the domain wall breaking the ordering. The domain walls separating the two domains consist almost exclusively of type 2 vertices, except for one type 3 vertex below the square hole. The upper domain wall winds a bit back and forth, while the domain wall in the lower right corner follows a straight diagonal. The image has been shaded corresponding to the two different magnetic domains present in the structure. The blue domain of the experimental image (figure 4.11b) has the same degenerate ground state as the simulated ground state in figure 4.11a. This can be seen by for example comparing the lower edge. The alternating black and white contrast regions are similar along the lower edge, but when passing the domain wall on the right side into the orange domain, the parity switches and the alternating black and white regions are now opposite of the simulation. This clearly exemplifies the difference between the two possible

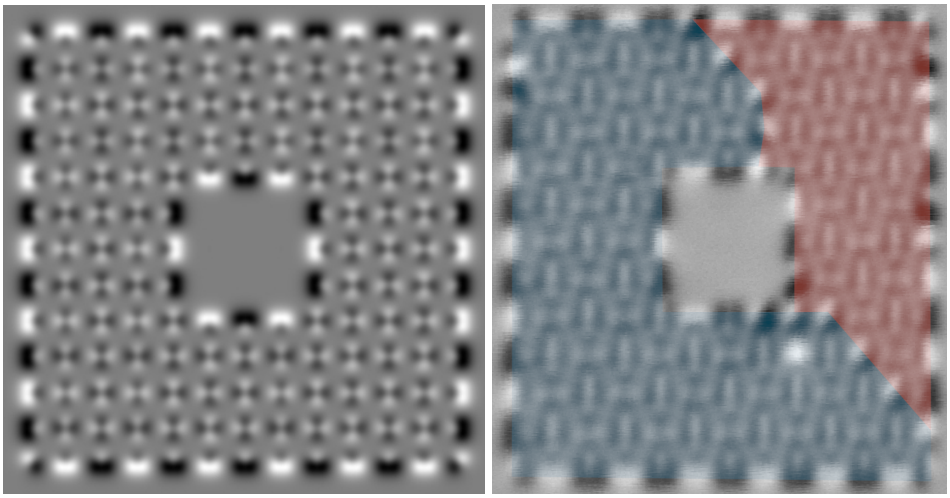

(a) **(b)**

Figure 4.11: (a) Simulated and **(b)** experimental MFM image of a 12×12 regular donut with a pitch of 295 nm and a lift height of 120 nm. The two domains in **(b)** are highlighted in different colors. Simulations were done using mumax3[24].

domains; the domains are equivalent, they are just shifted one magnet compared to each other.

The ground state ordering in the experimental images is not identical to the simulated MFM image. In the experimental images, the magnetization seem to "bleed" more, that is, fills in the regions between the vertices. This behavior could stem from a number of things, including low resolution due to the tip, local differences in magnetization stemming from the magnets not being completely single-domain, distortion, external vibrations and disturbances.

Figure 4.12 shows a 72×72 regular donut, shaded with colors corresponding to different domains. In the image there are domain walls stretching from the outer edge to the inner square, as well as domain walls starting and ending at the edge of the structure. There is an important difference between the two: Domain walls stretching from the inner square to the outer edge have to obey the previously mentioned parity rules, while domain walls starting and ending up on the same edge add an even number of domain wall nucleation sites to the rim that they are attached to. Thus, if there is already an odd number of walls connected the number will still be odd, and if there is already an even number it will still be even, and there is no issue with parity.

For some of the smaller domain walls residing along the edge in figure 4.12 it can be difficult to separate them from clusters of singular defects. In this work, the chains of type 2 vertices were not defined as domain walls if they did not encompass any ground state area. These were therefore not colored in the figure.

Studying the bottom line of the empty square in the middle more closely, an almost perfect pattern of every second dot being black and white emerges, with

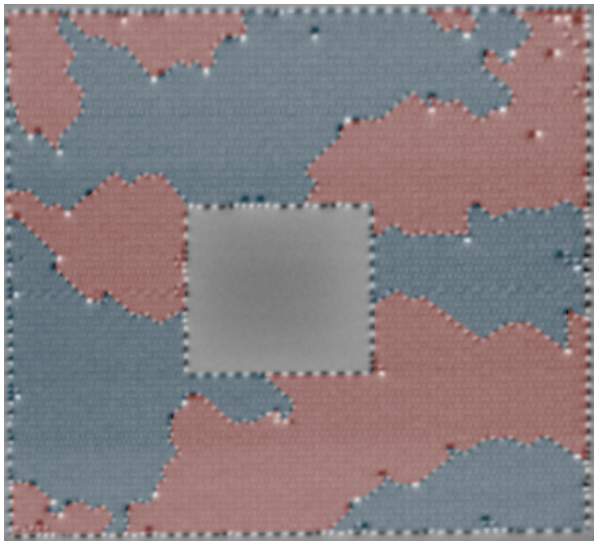

Figure 4.12: As-grown images of a 72 × 72 regular donut, highlighted to show the different domains.

the exception of a double black dot where the domain wall attaches to the central square edge. The other sides and the external edge are more irregular, but as this is a regular donut with no lattice defect, the total number of discrepancies from the expected ordering along the inner edge must be an even number.

Figure 4.13 shows an image of the 108 × 108 modified donut. There are three different colors needed to color the regions, even though there are only two types of domain present. This is due to the topological lattice defect, as explained in section 3.1. The modified region can be thought of as a bridge, connecting the two domains but not being part of either, and simultaneously being part of both.

The different lattice spacing and the transition area is hard to spot in larger structures compared to smaller ones. In a 108 × 108 modified donut with an original lattice spacing of 305 nm, the lattice spacing in the modified region will be 314 nm. This 9 nm difference in lattice spacing is small and thus hard to spot. There are 3 domain walls stretching from the inner square to the outer rim in this structure, which is a sign that there must be a lattice defect present.

The smallest donuts are made of 12×12 magnets. The modified region is much clearer in these images, as can be seen in figure 4.14. For the 12 × 12 donut with a lattice spacing of 295 nm, the modified lattice spacing becomes 393 nm, while the 12 × 12 donut with 305 nm lattice spacing has a modified lattice spacing of 407 nm, as shown to the left in table 3.1. As the differences are approximately 100 nm, it makes sense that these regions will have a much larger impact than they do in the larger structures, where the difference can be as low as 8.4 nm.

The larger contrast makes it more challenging to immediately decide whether there is a domain wall present or not. From the parity rule we know that there must be an odd number of domain walls present in the structure, and since there

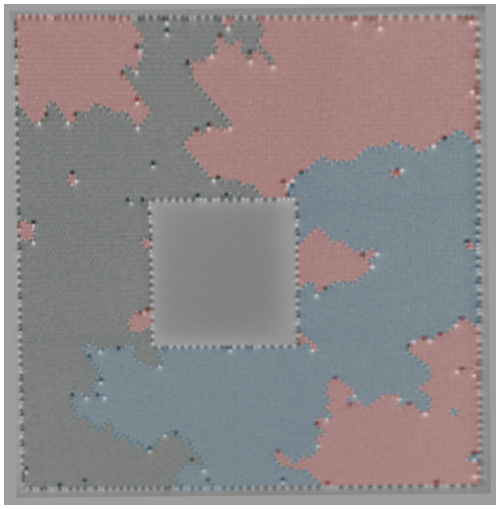

Figure 4.13: As-grown MFM image of a 108 × 108 modified donut, highlighted to show the different domains.

are two clearly shown domain walls in both images, it is expected that there is either one or three domain walls in the region with changed lattice spacing. Although it is not trivial to immediately spot the domain wall(s), the types of vertices are still recognizable. By analyzing these, it becomes clear that the structure with a pitch of 295 nm shown in figure 4.14a has one domain wall, while the structure with a pitch of 305 nm shown in figure 4.14b has one regular domain wall, and two rows of type 2 vertices right next to each other.

For most donut sizes, there are more domain walls in the modified than in the regular donuts, with one exception, as shown in figure 4.15. The total number of domain walls across sizes is still significantly higher in the modified structures. The difference between the total number of domain walls is 13, which corresponds to 1.3 domain walls extra per modified structure, on average. As the modified donuts must have at least 1 domain wall, as opposed to the regular which may have 0, it seems reasonable that the average difference in number of domain walls should be close to 1. The remaining 0.3 could correspond to domains being more easily created in the modified region due to the larger lattice spacing.

The domain walls are mostly diagonal, however, some smaller regions are horizontal or vertical. Figure 4.16a shows a segment of a 36×36 modified donut that has both diagonal and vertical domain wall sections. Primarily diagonal aligning with a few vertical sections interfering was also seen in simulations.

Domain walls consist primarily of type 2 vertices. These have a net magnetization pointing in a diagonal direction, as seen in figure 4.16. The large proportion of type 2 vertices in a diagonal ordering compared to horizontal or vertical ordering are pointing to this being a preferred aligning. It would make sense that the aligning in figure 4.16c would be less energetically favorable than the aligning in figure 4.16b, since the magnetic moments are tilted, and thus more frustrated.

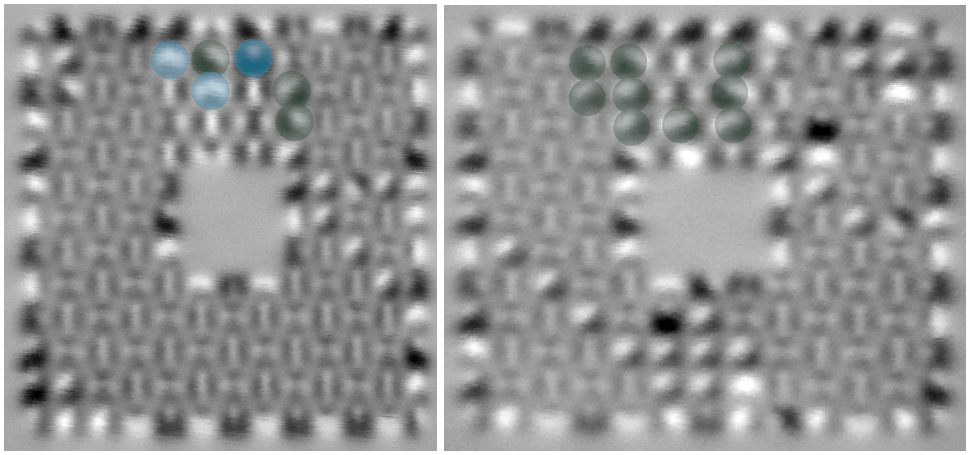

(a) **(b)**

Figure 4.14: A 12×12 modified donut with a pitch of **(a)** 295 nm and **(b)** 305 nm. Both are highlighted with green circles encompassing type 2 vertices and blue circles encompassing type 3 vertices in and around the modified region.

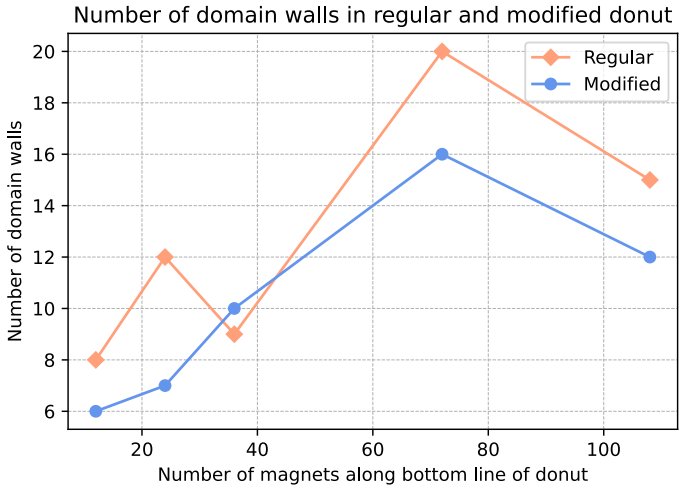

Figure 4.15: Number of domain walls in regular and modified donut structures. Both domain walls spanning from the inner hole to the outer edge and looping domain walls are counted. The total number of domain walls in the regular donuts are 51, and the modified donuts contain 64.

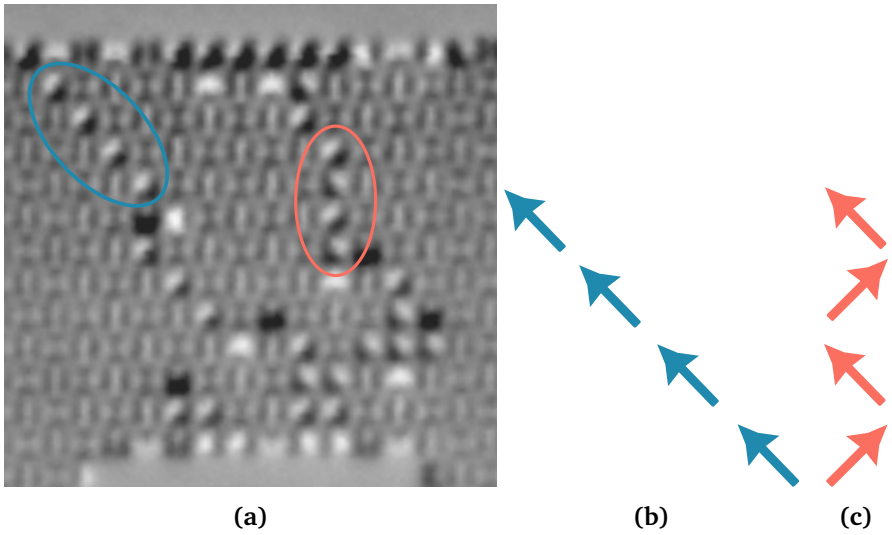

Figure 4.16: (a) A segment of a 36 × 36 modified donut. Two domain wall configurations are highlighted; to the left, a blue diagonal domain wall, and to the right, an orange vertical domain wall. Schematic representations of the magnetic moments of type 2 vertices of a **(b)** diagonal and **(c)** vertical domain wall are shown. Note that the vectors represent the magnetic moment of the type 2 vertices, not of the individual magnets.

This can be visualized by comparing the distance between the similar end of two different vectors. In the diagonal configuration, these repulsing ends will be further away from each other than in the vertical configuration, thus leading to less frustration.

All images obtained show a variety of defects. Figure 4.17 shows the correlation of number of defects and number of domain walls for all as-grown structures. The plot shows a clear correlation between the number of domain walls and the number of defects in a sample. A concrete example can be seen in figure 4.12, where multiple type 3 vertices can be seen in the domain walls. A smaller number of single-magnet defects can also be seen in the ground state ordered regions. Finding most of the defects in the domain walls was expected, because the energy barrier to change a type 2 vertex to a type 3 is much lower than changing a type 1 vertex to a type 3. The correlation plot shows that this holds for the obtained data. Both domain walls and defects arise from magnets having switched compared to the ground state. An important difference is that domains in as-grown samples have local ground states. If parts of a sample was initialized in one of the two degenerate ground states, and another part was initialized in the other ground state, the sample would have to form a domain wall between these regions. Removing this domain wall entirely would mean that all magnets in one of the two domains would have to switch. To remove a single-magnet defect, only one magnet has to switch. Thus, after fabrication, changes in single-magnet defects are much more likely than changes in the number of domain walls present.

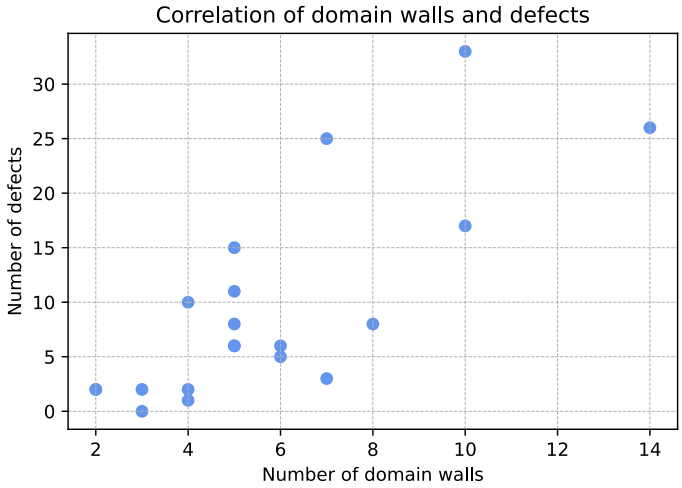

Figure 4.17: Number of domain walls plotted against number of defects for the as-grown structures studied in this project.

4.4.4 Lattice spacing

The studied structures have two different lattice spacings, 295 nm and 305 nm. The lattice spacings do not affect the dipole-dipole coupling between the magnets directly, but an increased lattice spacing will also increase the nearest neighbor spacing. The nearest neighbor spacing, which is the closest distance between the two closest magnets, is related to the dipolar coupling by a power of -3, as seen in equation 2.7.

Figure 4.18 shows the total number of defects for different sizes and lattice spacings. The smaller lattice spacing has less defects present than the larger. This difference gets bigger for larger structures. For the two largest structures, the number of defects is roughly half in the smaller lattice spacing, compared to the larger spacing.

Structures with larger lattice spacing have more domain walls and defects. This makes sense, as larger lattice spacing between the magnets give weaker dipole-dipole coupling. Weaker coupling will mean that the magnets are less "stuck", and thus switch more easily. The same effect was also seen in simulations of the coupling constant α. For smaller α, a weaker field was needed to switch magnets.

In figure 4.19, the number of defects in the modified region is shown for modified and regular donuts. For given sizes, two of the structures have more defects in the regular structure, and two have more defects in the modified structure. The total number of defects in the modified area in modified donuts is significantly larger than the regular donut. An important point to remember when discussing the modified region is that it is only the horizontal lattice spacing that has changed. This means that the nearest neighbor spacing has not changed as much as when comparing different structures with different lattice spacings. All the modified lat-

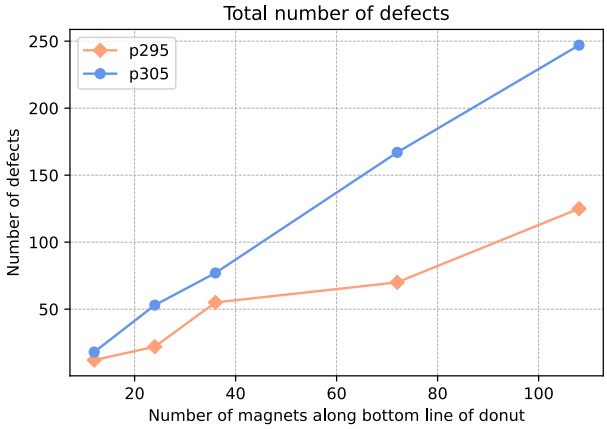

Figure 4.18: Total number of defects for different sized donuts and different pitch.

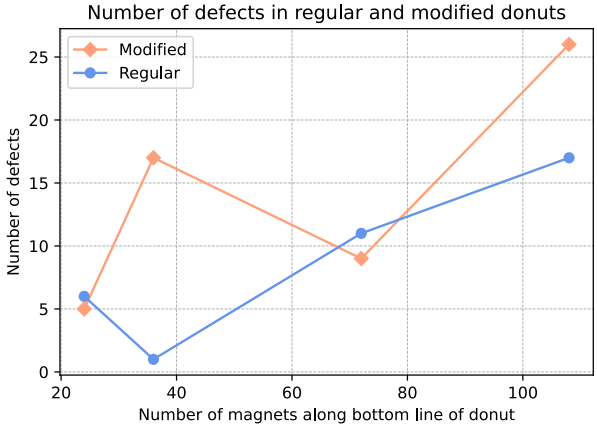

Figure 4.19: Number of defects in the modified region for modified and regular donuts.

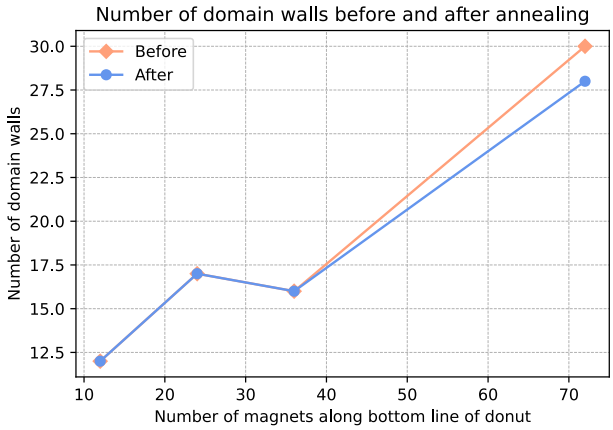

Figure 4.20: Number of domain walls before and after annealing.

tice spacings and nearest neighbor spacings are shown in table 3.1. As mentioned, the dipole-dipole interactions are related by r^{-3} to the nearest spacings. These interactions are weaker in the modified region, where the magnets are further apart. As the interactions are weaker, the magnets are more "free" to switch, as was seen for the structures with larger lattice spacing as well.

In the 12×12 modified donut structures seen in figure 4.14, it can be challenging to separate the magnetic defects from the domain walls in the area with increased lattice spacing. These two structures are therefore not included in statistical representations that count the number of defects. This can for instance be seen in figure 4.19, where the smallest structure recorded is 24×24.

4.4.5 Annealing

After the sample was annealed at 300 °C for 4 minutes and then 400 °C for 5 minutes, changes in magnetization were observed. The overall number of domain walls did not change much, as shown in figure 4.20. The only complete relaxing of domain walls was seen for the largest structures imaged after annealing, the 72×72 donuts, where two domain walls disappeared. However, multiple changes in magnet defects were observed.

A 24×24 donut is shown in figure 4.21 with some of its changes during annealing circled. The blue circles are showing relaxing motions going from higher order to lower order vertices. These are to be expected during an annealing process. The middle blue circle shows multiple magnet defects relaxing, and the blue circle furthest to the left shows a single-magnet defect disappearing during annealing. The orange circles are showing examples of single-magnet defects that appeared during annealing. The blue circle to the right is showing part of a domain wall, with changed magnetization after annealing. This change can be viewed as the domain wall shifting upwards. It is however very possible that the change is a single magnet switching, relaxing a neighboring magnet and thus giving the

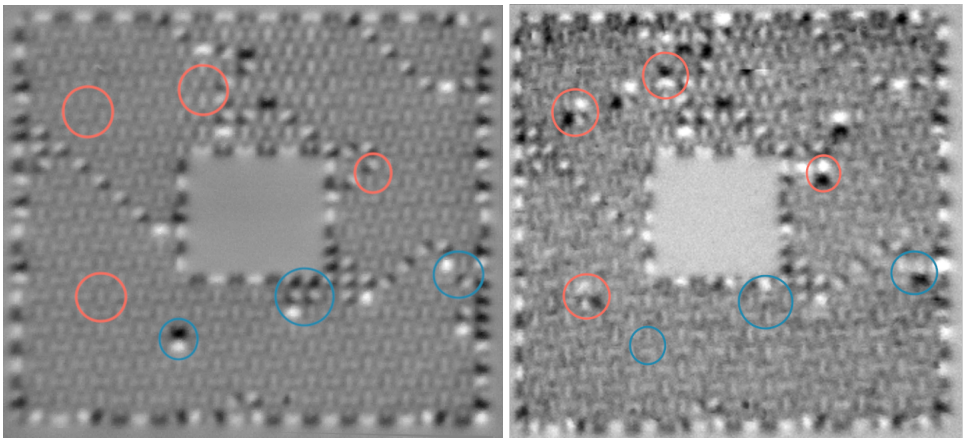

(a) **(b)**

Figure 4.21: A 24×24 modified donut with a pitch of 305 **(a)** before and **(b)** after annealing. The blue circles denote some of the defects or domain wall segments that disappeared during annealing, while the orange circles denote some of the defects or domain wall segments that appeared during the annealing process.

appearance of a shifting domain wall.

Perhaps more surprising is the appearance of single-magnet defects after annealing. The increase in temperature and fluctuations make switching of magnets more likely, and is therefore done to lower the switching energy barrier for the magnets so that they will relax into their ground state configuration more easily. However, the increase in thermal energy of the magnets make all kinds of switching more likely. Although the appearance of single defects cannot be explained by lowering of the interaction energy, local disturbances or random switching is more likely under heated conditions[25].

There is a difference in contrast between the two images, where the ground state seems to have stronger contrast in figure 4.21b than in figure 4.21a. This does not necessarily reflect actual change in magnetization between the images. Quantization of contrast in MFM images is almost impossible, due to external factors influencing the measurement.

The difference in number of defects before and after annealing is shown in figure 4.22 for six selected structures. There is a significant number of defects appearing during annealing in the structures with large lattice spacing. However, in the structures with small lattice spacing, the trend is opposite; there are fewer defects than before annealing. It is expected that less changes in defects will happen with smaller lattice spacings, from previous discussions of α. However, the overall reduction of defects only happening for smaller pitched structures is unexpected. It can be theorized that a higher α might "force" a ground state, however, the opposite behavior was seen for simulated domain wall movement, where a higher alpha led to more movement. It is possible that the combination of a high α and a high temperature during annealing led to a relaxing of the structure.

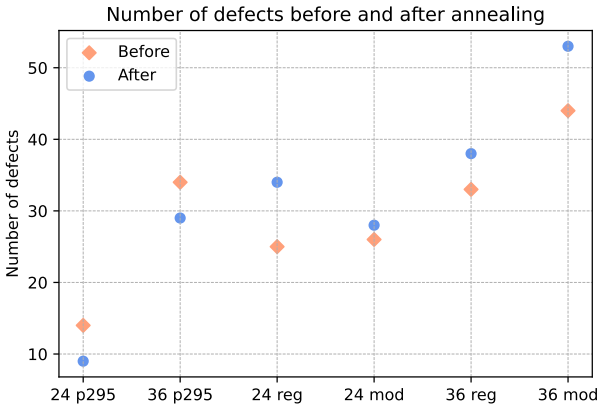

Figure 4.22: Number of defects before and after annealing for six selected structures. The structures were selected based on image quality. The structures are a 24 × 24 modified donut with a pitch of 295 nm, a 36 × 36 modified donut with a pitch of 295 nm, and regular and modified 24 × 24 and 36 × 36 donuts with a pitch of 305 nm.

The magnets in sample *B* were 25 nm thick. Thick magnets require more heat to switch than thinner magnets. To induce more switching of magnetization from heating at a given temperature, thinner magnets will be more suited. This behavior was also seen for lower alphas during preliminary simulations, where a lower field value was needed to start switching magnets with a smaller α.

Although some defects present before annealing were removed, a large number of new defects appeared. Especially curious was the high number of magnet defects appearing along horizontal, diagonal and other straight lines, as seen in figure 4.23. As mentioned, when annealing a sample, the expected result would be that single-magnet defects would disappear rather than appear. In addition, multiple single-magnet defects appearing in straight lines is not common, and energetically unfavorable. Thus, it seems unlikely that these rows of magnets would appear from random stochastic switching of single magnets.

The magnetic tip of the MFM can be used for writing magnetic states, as mentioned in section 2.5, by scanning across the sample in contact AFM mode. The observed lines do not always follow the scan direction of AFM scans. It is possible that the observed horizontal lines can have been written during AFM scanning, but the other lines of defects are stemming from something else. One of the techniques used while looking for samples described in section 3.4.1 utilizes contact AFM mode to look for samples while scanning in all kinds of directions. This type of multi-directional movement matches with the lines seen in the images. The magnet defect lines do not stretch across the sample, but rather appear and then disappear unpredictably. If the magnet defects arise from multi-directional contact AFM mode scans, the uneven writing would make sense, as the feedback loop is responding to uneven changes in the material. When scanning, a low scan speed

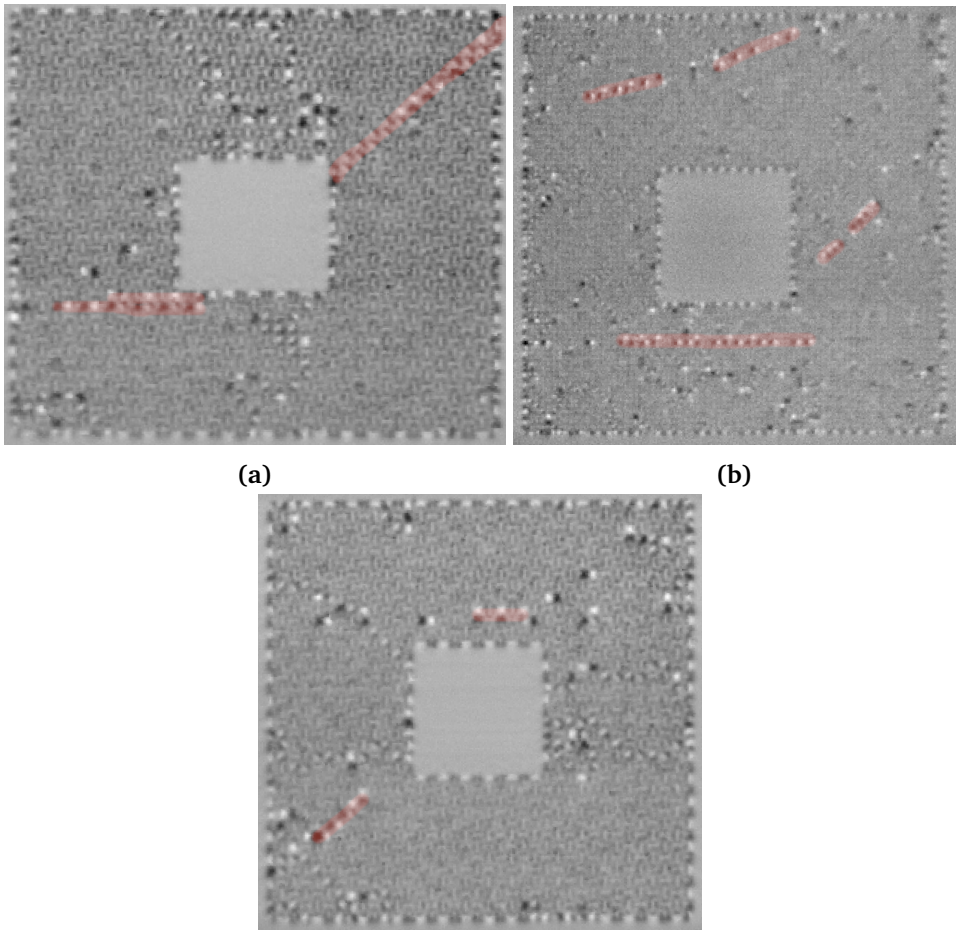

(a) **(b)**

(c)

Figure 4.23: (a) A 36 × 36 modified donut, **(b)** a 72 × 72 modified donut, and **(c)** a 36 × 36 regular donut after annealing. The highlighted orange areas show sequences of single magnet defects that appeared during the annealing process.

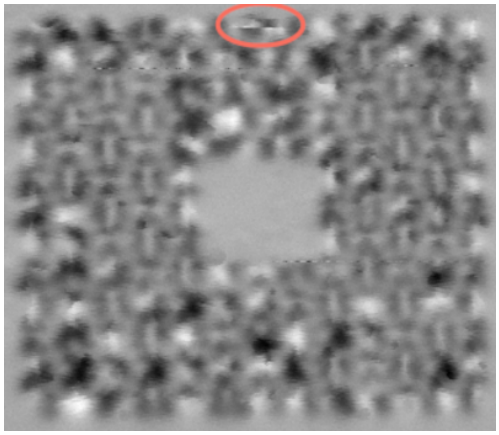

Figure 4.24: A 12 × 12 modified donut. Image taken at a lift height of 60 nm. In the highlighted area, there is a change of contrast across one of the magnets as the sample is scanned.

is utilized to avoid this exact problem. When moving back and forth, however, the MFM utilizes a slightly higher speed. This speed increase makes the movement and the height of the cantilever more unpredictable, with loss of control for the operator. The lack of control and increased speed, and the shape of the magnet defect rows, point to the MFM tip having induced this magnetization in the sample. This is something to be aware of for users operating an MFM. A safer way of searching for areas of interest is utilizing another searching technique, such as taking quick MFM pictures at a high lift height.

Knowing that these magnet defects most likely stem from MFM tip writing, statistics could theoretically be presented omitting these written lines, and thus providing an accurate analysis of what happened during analysis. However, the uneven response of the tip when being operated at such high speed, and the fact that there are rows of three or less magnet defects seemingly stemming from MFM writing in some of the images (shown in figure 4.23c), make it seem possible that the tip could have written separated single-magnet defects as well. This makes it difficult to know which magnet defects were induced by the tip. The change in defects for the structures with a lattice spacing of 295 nm might be the most accurate analysis, as they show no signs of writing. They show few induced single-magnets overall, but multiple single-magnet defects that were relaxed into the ground state. This is expected behavior during annealing procedures.

In the image of a 12 × 12 structure shown in figure 4.24 aquired at a lift height of 60 nm, the orange circle highlights a magnet that has black contrast on the left side and white contrast to the right for the first couple of scan rows. Then the magnetization switches, and there is white contrast to the left and dark contrast to the right. At the upper edge of the sample it then looks like the magnet switches back. As mentioned in section 2.5, when the tip-sample separation is more than 5 nm to 10 nm, writing is not expected to occur. However, it looks like this is exactly

what is seen in figure 4.24. Bad slope compensations and external factors such as vibrations can make the actual tip-sample distance be lower than the lift height. As the effect is only seen in the upper part of the figure, it seems likely that bad slope compensation in the y direction might play a part. The MFM slope compensation tool was found to be unpredictable at times, possibly because the sample was mounted slightly slanted onto the sample holder.

Writing magnetization using MFM can be used as an advantage to tune samples to wanted magnetic states, however, in this particular case it made it more difficult to correctly analyze the obtained data. A solution to the problem could be to record the images at a higher lift height, which in turn would most likely reduce the magnetic contrast.

Chapter 5

Conclusion

In this project, square artificial spin ices (ASIs) were studied, with the aim of understanding domain and defect formation in magnetic metamaterials. To analyze domain formation, ASIs were fabricated in the shape of a square annulus. This caused domain walls to form around the central square hole. A region with modified lattice spacing was introduced in the top central square of some of the structures. These "modified donuts" were studied both by simulations using flatspin[8] and by magnetic force microscopy (MFM) imaging of physical samples.

Both the physical systems and the simulations showed a tendency of the domain walls to order diagonally, and followed a set of "parity rules": All the regular donuts had an even number of domain walls, while the modified donuts had an odd number of domain walls. The number of domain walls in a structure was higher for structures with larger lattice spacing and thus less coupling between the magnets. The coupling affects the switching of magnets, in that a stronger coupling makes it harder for magnets to start switching. This was shown for square ASI structures under an applied field in simulations, and by comparing the number of defects in physical donuts with different lattice spacing.

Simulating systems with different coupling parameters showed that a stronger coupling made it possible to move or create domains by applying a global uniform magnetic field across the structure. This was difficult to do controllably, and the presence of different lattice spacings complicated the domain wall analysis.

Two samples, sample *A* and *B*, with magnet thicknesses of respectively 10 nm and 25 nm, were fabricated for analysis. Samples were analyzed using MFM. MFM is a practical tool for imaging small magnetic systems, however, if one is not careful, the magnetized tip of the cantilever used for scanning can write unwanted magnetic states into the material. This might interfere with other types of analysis, such as domain wall or defect counting.

The magnets in the ASIs need to be uniform enough that they exhibit monodomain behavior. If not, MFM analysis will show diffuse magnetic contrast, as was the case for sample *A*. MFM analysis of sample *B* showed a range of domain walls and defects. Single-magnet defects appear more often along domain walls and in structures with large lattice spacing. By annealing the sample, we can relax some

of these single-magnet defects into a ground state ordering of type 1 vertices.

More research and knowledge about ASI as a metamaterial and its possible applications is necessary to further advance it as a candidate for physical reservoir computing.

Further work

Initial examinations of this specific square ASI structure are promising for understanding frustration and domain wall properties, however, the ultimate goal of moving the domain walls controllably by applying a certain magnitude of field was not achieved. It is possible that this could be done by testing more field protocols and tuning parameters, however, after initial investigations this seems unlikely. Future simulations should be performed on a larger system with disorder, and with a physically realizable α, to more closely mimick physical systems.

Another option going forward would be to investigate physical samples more thoroughly and applying a field, maybe even in combination with a set temperature, to promote switching. Introducing the topological defect in the modified donut structure can be done in multiple different ways. By designing the structures differently, for example by rotating magnets to compensate for missing rows instead of changing the lattice spacing, the problems that arose from the large lattice spacing can be avoided. If the goal is to have magnets switch at low applied field strengths a thinner sample will be beneficial, while a thicker sample will give more rich dynamics of magnetic domains under a high applied field.

The statistics presented in this paper are based on counting domain walls and other type 2 and 3 vertices manually from the images shown in appendix 5. Statistics on the number of defects were included to show trends and compare structures, which could be done since all the structures were counted in the same way. Developing a method to analyze the types of vertices computationally could be advantageous for future research, as it would remove the human error aspect, as well as be more efficient for larger numbers of images. A more exact analysis would be to base the statistics on vertices, rather than separating between domain walls and non-domain walls. If vertices were counted instead of defects and domain walls, this would lead to a high count of type 2 vertices, as all the long domain walls would be broken town into its components, which are mainly type 2 vertices. The length of domain walls is not part of the analysis done in this thesis. For future work, it could be interesting to see what influences the length of domain walls, and how strongly correlated it is to the number of domain walls. Counting domain walls and defects in 20 structures that are all slightly different is statistically a small amount of data. More data is needed to corroborate the trends presented in this thesis, especially those pertaining to only a small number of the investigated structures.

Bibliography

[1] G. Holm, *Domain wall movement in defect artificial spin ice*, Project Thesis at the Department of Electronic Systems, Dec. 2022.

[2] W. Van Heddeghem, S. Lambert, B. Lannoo, D. Colle, M. Pickavet and P. Demeester, 'Trends in worldwide ICT electricity consumption from 2007 to 2012,' *Computer Communications*, vol. 50, pp. 64–76, Sep. 2014, ISSN: 01403664.

[3] S. Kumar, 'Fundamental Limits to Moore's Law,' Stanford University, Stanford, Tech. Rep., Nov. 2015.

[4] G. Tanaka, T. Yamane, J. B. Héroux, R. Nakane, N. Kanazawa, S. Takeda, H. Numata, D. Nakano and A. Hirose, *Recent advances in physical reservoir computing: A review*, Jul. 2019.

[5] J. H. Jensen, E. Folven and G. Tufte, 'Computation in artificial spin ice,' 2018.

[6] S. H. Skjærvø, C. H. Marrows, R. L. Stamps and L. J. Heyderman, 'Advances in artificial spin ice,' *Nature Reviews Physics*, vol. 2, no. 1, pp. 13–28, Jan. 2020, ISSN: 25225820.

[7] R. Puttock, I. M. Andersen, C. Gatel, B. Park, M. C. Rosamond, E. Snoeck and O. Kazakova, 'Defect-induced monopole injection and manipulation in artificial spin ice,' *Nature Communications*, vol. 13, no. 1, Dec. 2022, ISSN: 20411723.

[8] J. H. Jensen, A. Strømberg, O. R. Lykkebø, A. Penty, J. Leliaert, M. Själander, E. Folven and G. Tufte, 'flatspin: A large-scale artificial spin ice simulator,' *Physical Review B*, vol. 106, no. 6, Aug. 2022, ISSN: 24699969.

[9] Inkscape project, *Inkscape*, 2020.

[10] D. Nečas and P. Klapetek, 'Gwyddion: an open-source software for SPM data analysis,' *Open Physics*, vol. 10, no. 1, Jan. 2012, ISSN: 2391-5471.

[11] The GIMP Development Team, *GIMP*, Jun. 2019.

[12] J. M. D. Coey, *Magnetism and Magnetic Materials*. Cambridge University Press, Jan. 2009, ISBN: 9780521016766.

[13] M. Getzlaff, *Fundamentals of Magnetism*, 1st ed. Springer, 2008.

[14] C. Kittel, *Introduction to Solid State Physics*, 8th ed. Wiley, 2005.

[15] R. F. Wang, C. Nisoli, R. S. Freitas, J. Li, W. McConville, B. J. Cooley, M. S. Lund, N. Samarth, C. Leighton, V. H. Crespi and P. Schiffer, 'Artificial 'spin ice' in a geometrically frustrated lattice of nanoscale ferromagnetic islands,' *Nature*, vol. 439, no. 7074, pp. 303–306, Jan. 2006, ISSN: 14764687.

[16] A. P. Ramirez, A. Hayashi, R. J. Cava, R. Siddharthan and B. S. Shastry, 'Zero-point entropy in 'spin ice',' Tech. Rep., 1999.

[17] J. D. Bernal and R. H. Fowler, 'A theory of water and ionic solution, with particular reference to hydrogen and hydroxyl ions,' *The Journal of Chemical Physics*, vol. 1, no. 8, pp. 515–548, 1933, ISSN: 00219606.

[18] J. Drisko, T. Marsh and J. Cumings, 'Topological frustration of artificial spin ice,' *Nature Communications*, vol. 8, Jan. 2017, ISSN: 20411723.

[19] D. J. Gauthier, E. Bollt, A. Griffith and W. A. Barbosa, 'Next generation reservoir computing,' *Nature Communications*, vol. 12, no. 1, Dec. 2021, ISSN: 20411723.

[20] C. Tannous and J. Gieraltowski, 'The Stoner-Wohlfarth model of ferromagnetism,' *European Journal of Physics*, vol. 29, no. 3, pp. 475–487, May 2008, ISSN: 13616404.

[21] Y. Chen, *Nanofabrication by electron beam lithography and its applications: A review*, Mar. 2015.

[22] J. C. Gartside, D. M. Burn, L. F. Cohen and W. R. Branford, 'A novel method for the injection and manipulation of magnetic charge states in nanostructures,' *Scientific Reports*, vol. 6, Sep. 2016, ISSN: 20452322.

[23] J. C. Gartside, D. M. Arroo, D. M. Burn, V. L. Bemmer, A. Moskalenko, L. F. Cohen and W. R. Branford, 'Realization of ground state in artificial kagome spin ice via topological defect-driven magnetic writing,' *Nature Nanotechnology*, vol. 13, no. 1, pp. 53–58, Jan. 2018, ISSN: 17483395.

[24] A. Vansteenkiste, J. Leliaert, M. Dvornik, M. Helsen, F. Garcia-Sanchez and B. Van Waeyenberge, 'The design and verification of MuMax3,' *AIP Advances*, vol. 4, no. 10, Oct. 2014, ISSN: 21583226.

[25] X. Zhang, Y. Lao, J. Sklenar, N. S. Bingham, J. T. Batley, J. D. Watts, C. Nisoli, C. Leighton and P. Schiffer, 'Understanding thermal annealing of artificial spin ice,' *APL Materials*, vol. 7, no. 11, Nov. 2019, ISSN: 2166532X.

[26] M. Själander, M. Jahre, G. Tufte and N. Reissmann, 'EPIC: An energy-efficient, high-performance GPGPU computing research infrastructure,' Dec. 2019.

Appendix 1: MFM images of sample B

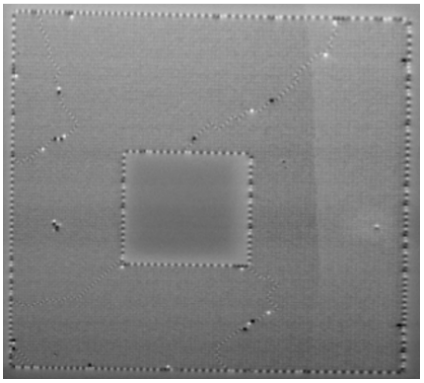

(a) 108 × 108 modified donut, pitch 295

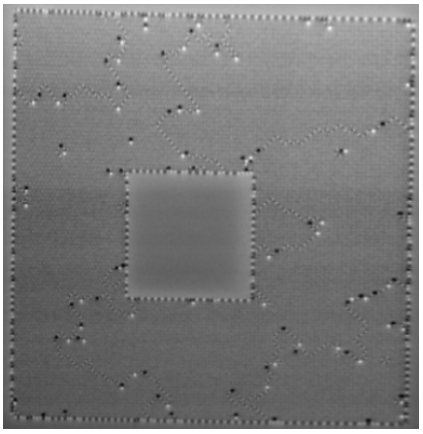

(b) 108 × 108 modified donut, pitch 305

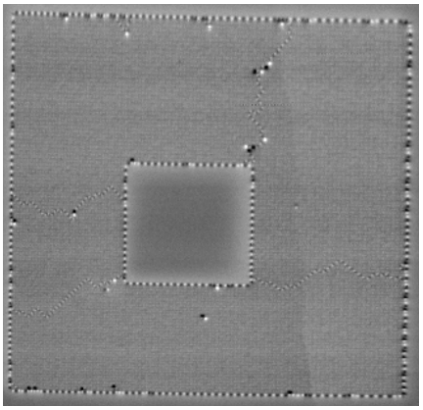

(c) 108 × 108 regular donut, pitch 295

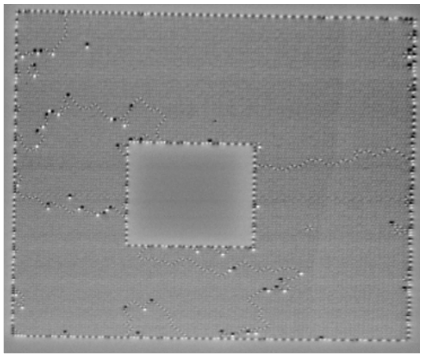

(d) 108 × 108 regular donut, pitch 305

Figure 1: 108 × 108 modified and regular donuts with different pitches, before and after annealing.

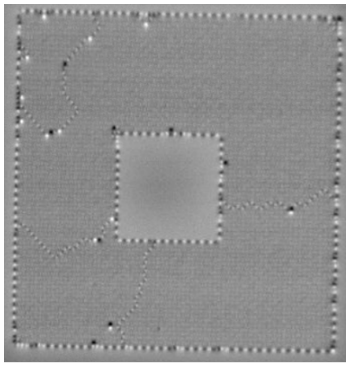

(a) 72 × 72 modified donut, pitch 295

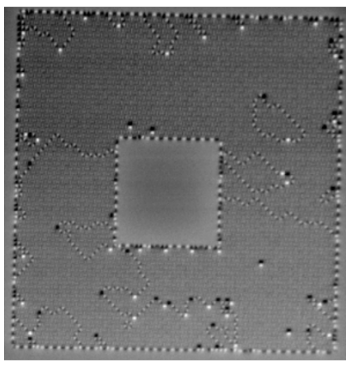

(b) 72 × 72 modified donut, pitch 305

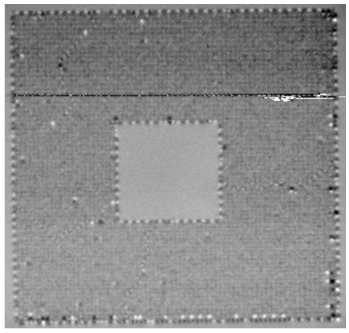

(c) 72 × 72 modified donut, pitch 295, after annealing

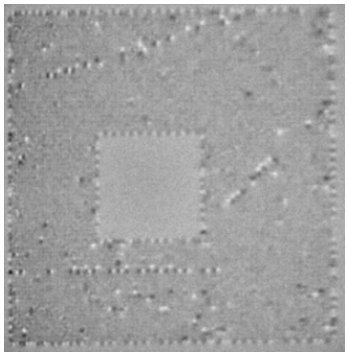

(d) 72 × 72 modified donut, pitch 295, after annealing

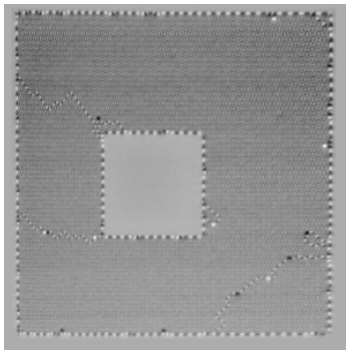

(e) 72 × 72 without defect, pitch 295

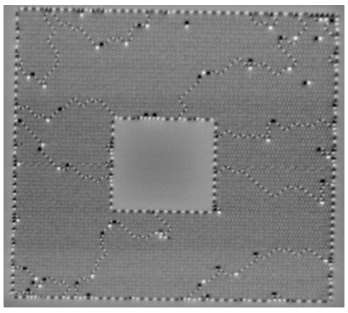

(f) 72 × 72 without defect, pitch 305

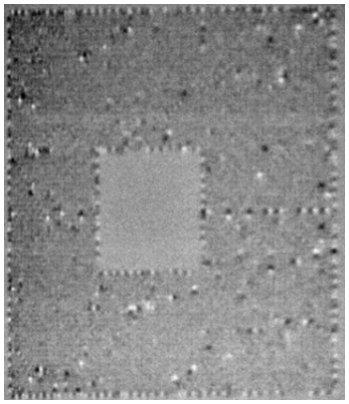

(g) 72 × 72 without defect, pitch 305, after annealing

Figure 2: 72 × 72 modified and regular donuts with different pitches, before and after annealing.

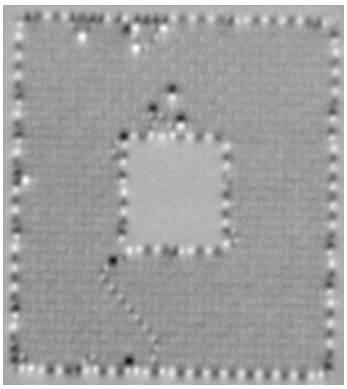

(a) 36 × 36 modified donut, pitch 295

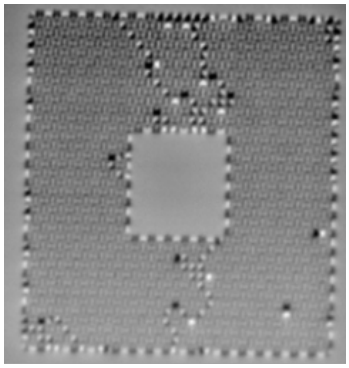

(b) 36 × 36 modified donut, pitch 305

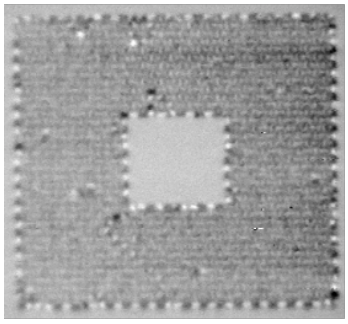

(c) 36 × 36 modified donut, pitch 295, after annealing

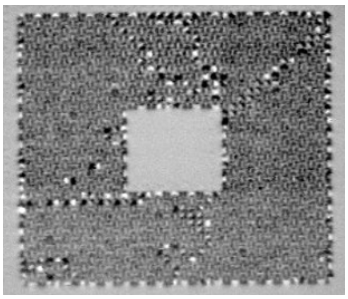

(d) 36 × 36 modified donut, pitch 295, after annealing

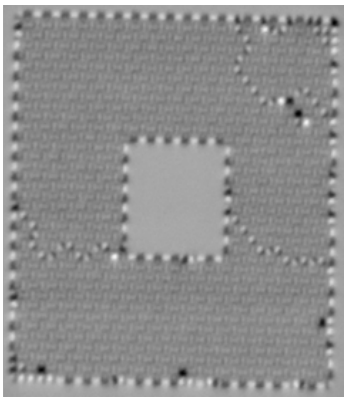

(e) 36 × 36 regular donut, pitch 295

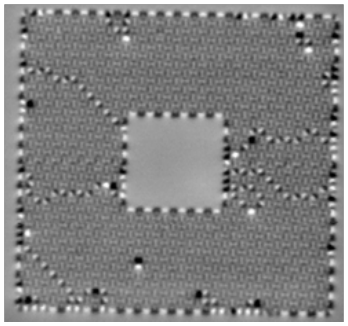

(f) 36 × 36 regular donut, pitch 305

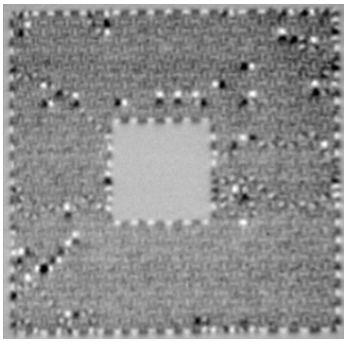

(g) 36 × 36 regular donut, pitch 305, after annealing

Figure 3: 36 × 36 modified and regular donuts with different pitches, before and after annealing.

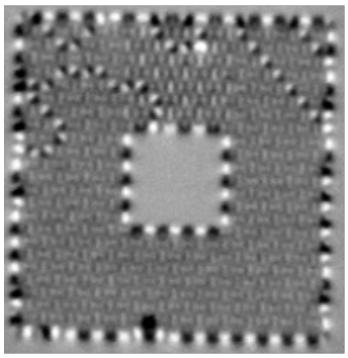

(a) 24 × 24 modified donut, pitch 295

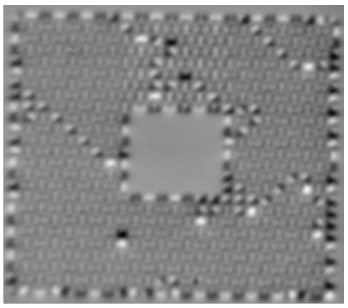

(b) 24 × 24 modified donut, pitch 305

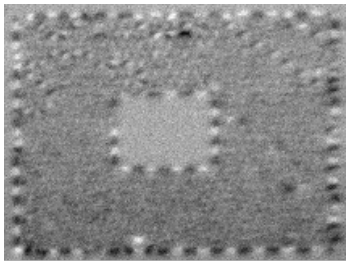

(c) 24 × 24 modified donut, pitch 295, after annealing

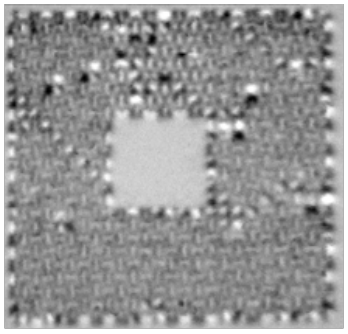

(d) 24 × 24 modified donut, pitch 295, after annealing

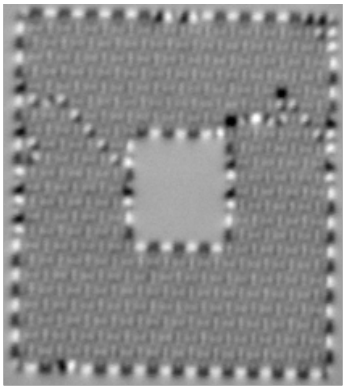

(e) 24 × 24 regular donut, pitch 295

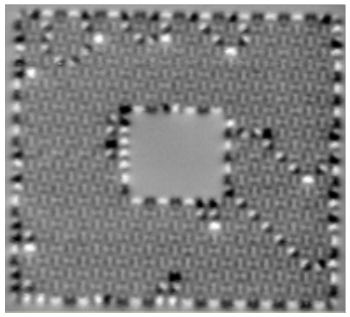

(f) 24 × 24 regular donut, pitch 305

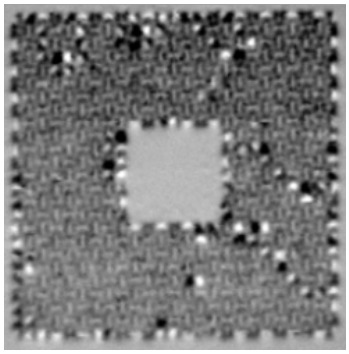

(g) 24 × 24 regular donut, pitch 305, after annealing

Figure 4: 24 × 24 modified and regular donuts with different pitches, before and after annealing.

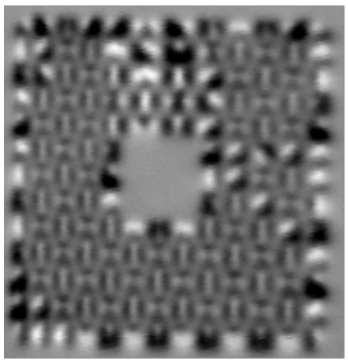

(a) 12 × 12 modified donut, pitch 295.

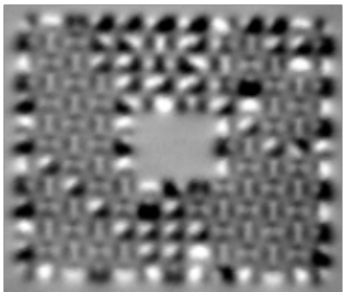

(b) 12 × 12 modified donut, pitch 305

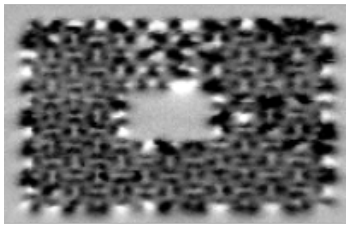

(c) 12 × 12 modified donut, pitch 295, after annealing

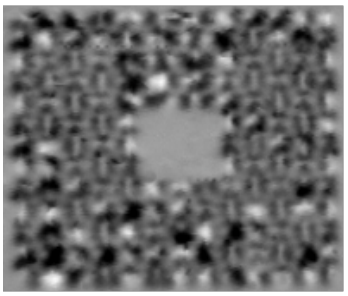

(d) 12 × 12 modified donut, pitch 295, after annealing

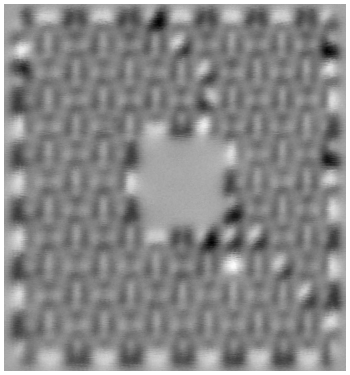

(e) 12 × 12 regular donut, pitch 295

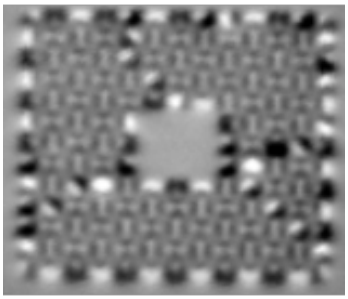

(f) 12 × 12 regular donut, pitch 305

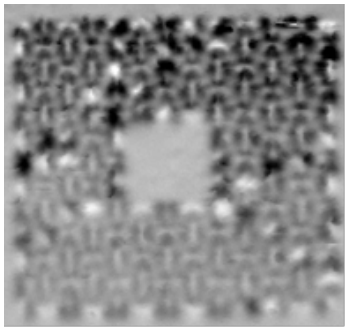

(g) 12 × 12 regular donut, pitch 305, after annealing

Figure 5: 12 × 12 modified and regular donuts with different pitches, before and after annealing.

Appendix 2: flatspin simulations

Structure	Size	Alpha	Angle(s)	Min.field	Max.field
Square ASI	8	0.0001	45	76	78
Square ASI	8	0.0005	0	68	100
Square ASI	8	0.0005	45	78	80
Square ASI	8	0.001	0	70	80
Square ASI	8	0.001	45	70	80
Square ASI	8	0.001	45	79	87
Square ASI	8	0.0015	45	95	96
Square ASI	8	0.002	0	75	84
Square ASI	8	0.002	45	64	91
Square ASI	8	0.002	45	70	82
Square ASI	8	0.002	45	101	103
Square ASI	8	0.002	135	68	90
Square ASI	8	0.002	315	64	91
Square ASI	8	0.002	315+315+45	89	89
Square ASI	8	0.002	45+45+0+0+315+315	74	89
Square ASI	8	0.002	45+45+315	89	89
Square ASI	8	0.002	45+45+315+315+0+0	89	89
Square ASI	8	0.002	45+45+315+45	89	89
Square ASI	8	0.0025	45	100	110
Square ASI	8	0.003	45	110	114
Square ASI	8	0.003	135	113	115
Square ASI	8	0.003	225	113	114
Square ASI	8	0.003	135+45	113	114
Square ASI	8	0.003	45+135	113	113
Square ASI	8	0.003	45+135+225	113	113
Square ASI	8	0.003	45+135+225+315	113	113
Square ASI	8	0.003	45+225	113	113
Square ASI	8	0.003	45+225+45	113	113
Square ASI	8	0.003	45+225+45+45	113	113
Square ASI	8	0.003	45+225+45+45+45	113	113
Square ASI	8	0.003	45+225+45+45+45+45	113	113
Square ASI	8	0.003	45+225+45+45+45+45+45	113	113
Regular donut	8	0.001	45	80	
Regular donut	8	0.001	45	84	
Regular donut	8	0.001	45	90	
Regular donut	8	0.003	45	100	
Regular donut	8	0.003	45	105	
Regular donut	8	0.003	45	108	
Regular donut	8	0.003	45	110	
Regular donut	8	0.003	45	112	

Regular donut	8	0.003	45	113
Regular donut	8	0.003	45	113.5
Regular donut	8	0.003	45	113.5
Regular donut	8	0.003	45	113.56
Regular donut	8	0.003	45	114
Regular donut	8	0.003	135	113.5
Regular donut	8	0.003	225	113
Regular donut	8	0.003	225	113.5
Regular donut	8	0.003	315	113
Modified donut	8	0.003	45	100
Modified donut	8	0.003	45	101
Modified donut	8	0.003	45	102
Modified donut	8	0.003	45	103
Modified donut	8	0.003	45	105
Modified donut	8	0.003	45	110
Modified donut	8	0.003	45	112
Modified donut	8	0.003	45	112
Modified donut	8	0.003	45	113
Modified donut	8	0.003	45	113.5
Modified donut	8	0.003	45	114
Modified donut	8	0.003	135	112.1
Modified donut	8	0.003	135	112.5
Modified donut	8	0.003	135	113
Modified donut	8	0.003	135	113
Modified donut	8	0.003	135	113
Modified donut	8	0.003	225	113
Modified donut	8	0.003	315	113

Table 1: flatspin simulations run. The simulations with both min and max field were run for all field values in between, in increments of 1 mT.

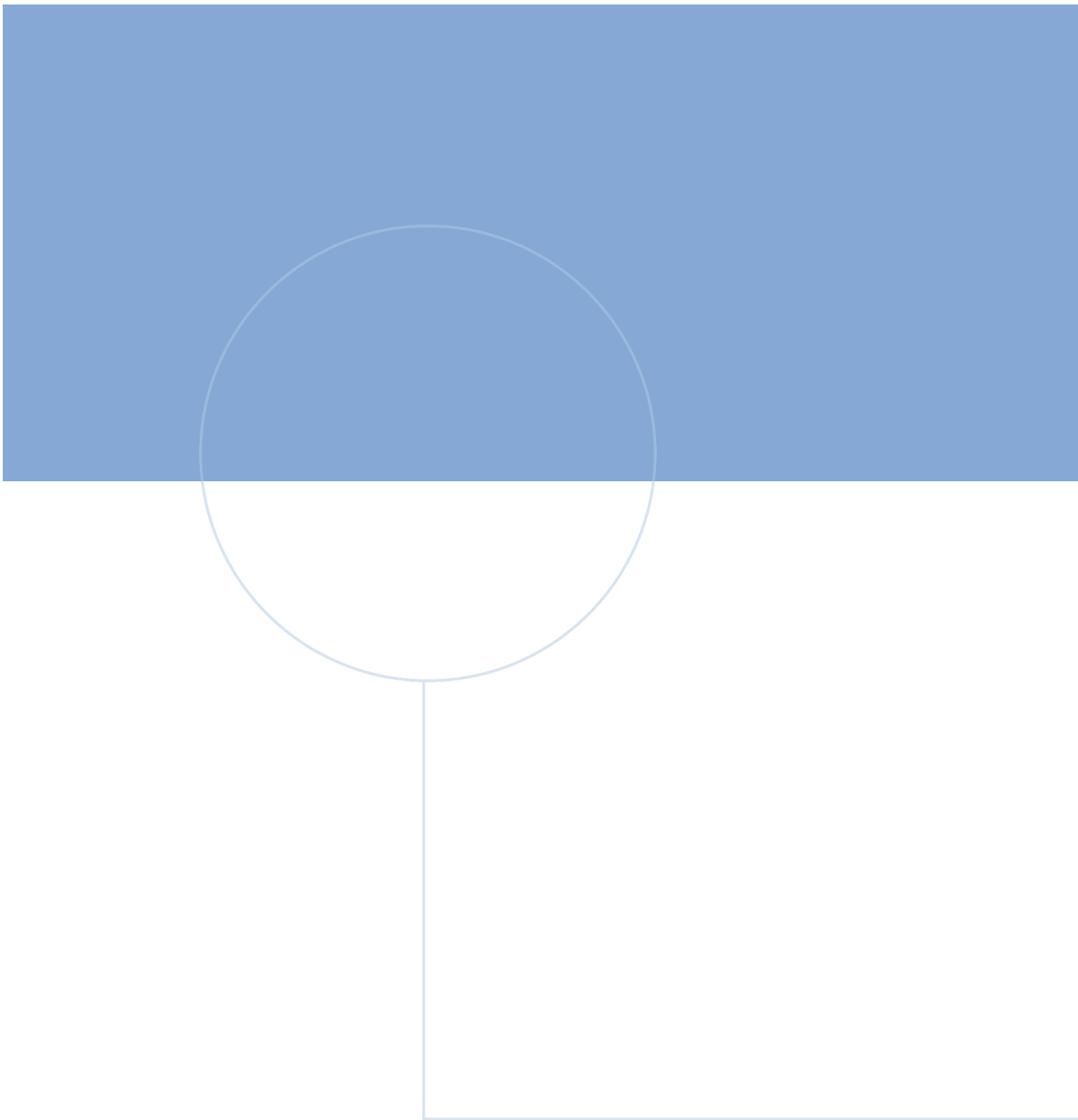

NTNU

Norwegian University of
Science and Technology